

The Accuracy of Morphological Decomposition of AGN Host Galaxies

B. D. Simmons and C. M. Urry

Astronomy Department, Yale University, New Haven, CT USA

simmons@astro.yale.edu

ABSTRACT

In order to assess the accuracy with which we can determine the morphologies of AGN host galaxies, we have simulated more than 50,000 ACS images of galaxies with $z < 1.25$, using image and noise properties appropriate for the GOODS survey. We test the effect of central point-source brightness on host galaxy parameter recovery with a set of simulated AGN host galaxies made by adding point sources to the centers of normal galaxies. We extend this analysis and also quantify the recovery of intrinsic morphological parameters of AGN host galaxies with a set of fully simulated inactive and AGN host galaxies.

We can reliably separate good from poor fit results using a combination of reasonable error cuts, in the regime where $(L_{\text{host}}/L_{\text{PS}}) > 1 : 4$. We give quantitative estimates of parameter errors as a function of host-to-point-source ratio. In general, we separate host and point-source magnitudes reliably at all redshifts; point sources are well recovered more than 90% of the time, although spurious detection of central point sources can be as high as 25% for bulge-dominated sources. We find a general correlation between Sérsic index and intrinsic bulge-to-total ratio, such that a host galaxy with Sérsic $n < 1.5$ generally has at least 80% of its light from a disk component. Likewise, “bulge-dominated” galaxies with $n > 4$ typically derive at least 70% of their total host galaxy light from a bulge, but this number can be as low as 55%. Single-component Sérsic fits to an AGN host galaxy are statistically very reliable to $z < 1.25$ (for ACS survey data like ours). In contrast, two-component fits involving separate bulge and disk components tend to over-estimate the bulge fraction by $\sim 10\%$, with uncertainty of order 50%.

Subject headings: methods: data analysis — galaxies: active — galaxies: nuclei — galaxies: bulges — galaxies: fundamental parameters

1. Introduction

Morphological analysis of two-dimensional light profiles of galaxies in large data surveys provides detailed information about galaxy populations and their evolution (*e.g.*, Simard et al. 1999; Ravindranath et al. 2004; Jogee et al. 2004; Sheth et al. 2008). Simulations of both large and small galaxy samples show that two-dimensional parametric and non-parametric morphological analysis of normal galaxies is extremely robust (Marleau & Simard 1998; Graham 2001; Conselice 2003; Trujillo & Aguerri 2004; Häussler et al. 2007).

Studies of active galactic nucleus (AGN) host galaxies give us the opportunity to study not just the galaxies themselves, but also the well-established connection between galaxies and central supermassive black holes (Kormendy & Richstone 1995; Magorrian et al. 1998; Ferrarese & Merritt 2000; Gebhardt et al. 2000; McLure & Dunlop 2002; Marconi & Hunt 2003). In cases where central black hole masses are independently determined, accurate decompositions of AGN host galaxies from their central point-source light contributions allow for the direct study of how galaxy light distribution relates to black hole properties. Alternatively, when time-intensive observations of black hole mass are not available, we can use established bulge-black hole relations to determine the black hole masses from bulge luminosities.

However, two-dimensional morphological fitting of AGN host galaxies is more complicated than that of “normal” (or “inactive”) galaxies because of the presence of a central point source, which is often quite bright. In order to extract host galaxy properties from a source comprised of a host plus a central AGN, spatial resolution is critical. Thus the Advanced Camera for Surveys (ACS) on the *Hubble Space Telescope* (*HST*) is the instrument of choice for many AGN host galaxy studies to date (Sánchez et al. 2004; Alonso-Herrero et al. 2008; Ballo et al. 2007).

Of the large multi-wavelength surveys currently available, the Great Observatories Origins Deep Survey (GOODS; Giavalisco et al. 2004) provides some of the deepest multicolor ACS data. AGN identification is possible because of deep X-ray imaging with *Chandra*, as well as ground-based optical and infrared spectroscopic follow up. *Spitzer* data provide additional information on total light but insufficient spatial resolution to separate the galaxy from the active nucleus. We performed detailed morphological analysis on the GOODS ACS data set using GALFIT (Peng et al. 2002), the results of which are presented in a forthcoming paper (B. D. Simmons et al. 2008, in preparation, hereafter S08). In order to understand the accuracy of those results – in particular, to probe the well-known effects of surface brightness dimming and dependence of physical resolution on redshift in the presence of a central point source whose size does not change with redshift – extensive simulations of host galaxy morphology are required.

Previously, Sánchez et al. (2004) simulated 1880 single-component host galaxies with point sources fainter than the host galaxy. Here we present a full treatment of over 50,000 simulated AGN host galaxies in the redshift range $0.1 < z < 1.1$, with both single-component and two-component bulge-plus-disk morphologies, and central point sources that are both brighter and fainter than the host galaxy. Results of these simulations are intended to inform data analysis of AGN host morphologies, to better infer intrinsic host galaxy shapes from fitted morphological parameters in the presence of a central point source.

We discuss the data from which we draw our noise properties and simulated sample in Section 2. The detailed fit procedures and the simulation parameter space are presented in Section 3, and we assess the ability of our fitting procedure to recover accurate host galaxy and point-source parameters from GOODS-like images of AGN host galaxies in Section 4.

2. Data

2.1. HST ACS Data

The GOODS fields each cover an area of approximately $10' \times 16'$ with a total of 398 *HST* orbits in both fields. The ACS has a resolution of $0''.05 \text{ pixel}^{-1}$, and observations were taken in the F435W, F606W, F775W, and F850LP ACS bands, hereafter referred to as *B*, *V*, *I*, and z' , respectively. Data acquisition and reduction are detailed in Giavalisco et al. (2004) and Koekemoer et al. (2002). Each of the five epochs of data was processed via the basic ACS pipeline and a further processing task called multidrizzle, which finds an astrometric solution for all 5 epochs in order to correct for geometric distortion, and at the same time removes cosmic rays from the image (Koekemoer et al. 2002). The final images have resolution of $0''.03 \text{ pixel}^{-1}$, and the magnitude limits for extended sources are $B < 28.4 \text{ mag}$, $V < 28.4 \text{ mag}$, $I < 27.7 \text{ mag}$, and $z < 27.3 \text{ mag}$.

From the reduced data, we randomly selected 450 inactive galaxies with stellarity class less than 0.8 (*i.e.*, objects that are not point sources) and magnitude $z' < 24.0 \text{ mag}$ for use in those of our simulations that include real data (§3.3). Since the majority of AGN host galaxies selected for morphological analysis in current surveys using *HST* have redshifts such that their *I*-band data lie in the rest-frame *B* band ($0.575 < z < 0.9$), we performed simulations using the *I*-band images and noise properties.

2.2. Noise Properties

For fully simulated galaxies (described in §3.4), noise appropriate to the GOODS-ACS fields was added. The task of simulating the noise in the GOODS-ACS fields is complicated by the dithering process, which correlates the noise among nearby pixels. We therefore use actual noise pixels (i.e., source-free pixels) from the final GOODS-N and GOODS-S images rather than statistical models. We sampled 150 sub-sections of the GOODS images that contained no sources, 75 in the North field and 75 in the South, for a total of over 2.5 million noise pixels. Each of these sub-sections was cut into tiles of size 50×50 pixels; this resulted in 1042 tiles. These were then used to create 500 noise images of the same size as our data images by arranging random mosaics of the 50×50 noise tiles. We have verified that these new noise mosaics have the same overall noise properties (distribution of pixel intensities) as the original noise-only subsections of the GOODS images (Figure 1).

We also tested noise mosaics created from 10×10 tiles of background noise but found that the distribution of pixel intensities was shifted compared to the correlated noise properties of the dithered ACS images. We thus used only the 50×50 pixel noise images to create our final noise mosaics. The noise value distributions of the 50×50 and 10×10 noise mosaics are compared to the actual GOODS noise distribution in Figure 1.

3. Creation and Morphological Fitting of Simulated Samples

We performed two distinct sets of simulations to test the accuracy of derived morphological parameters. First, we used a sample of 450 real galaxies from the GOODS fields and added point sources to their centers. This allowed us to test the ability of GALFIT to extract point sources from the centers of real galaxies. It also informed our choice of parameters and galaxy types for the second, more extensive, set of simulations. In the latter set of simulations, we created a sample of 12,592 completely simulated GOODS galaxies, in order to additionally test the recovery of a wide range of host galaxy parameters. We fitted all of our simulated galaxies with our batch-fitting algorithm (described below). We also simulated the redshifting of these galaxies to quantify redshift-dependent effects, and we added noise taken directly from real GOODS data.

3.1. Fit Procedure

We performed morphological analysis in two dimensions using GALFIT, which can simultaneously fit an arbitrary number of components to an image (Peng et al. 2002). The

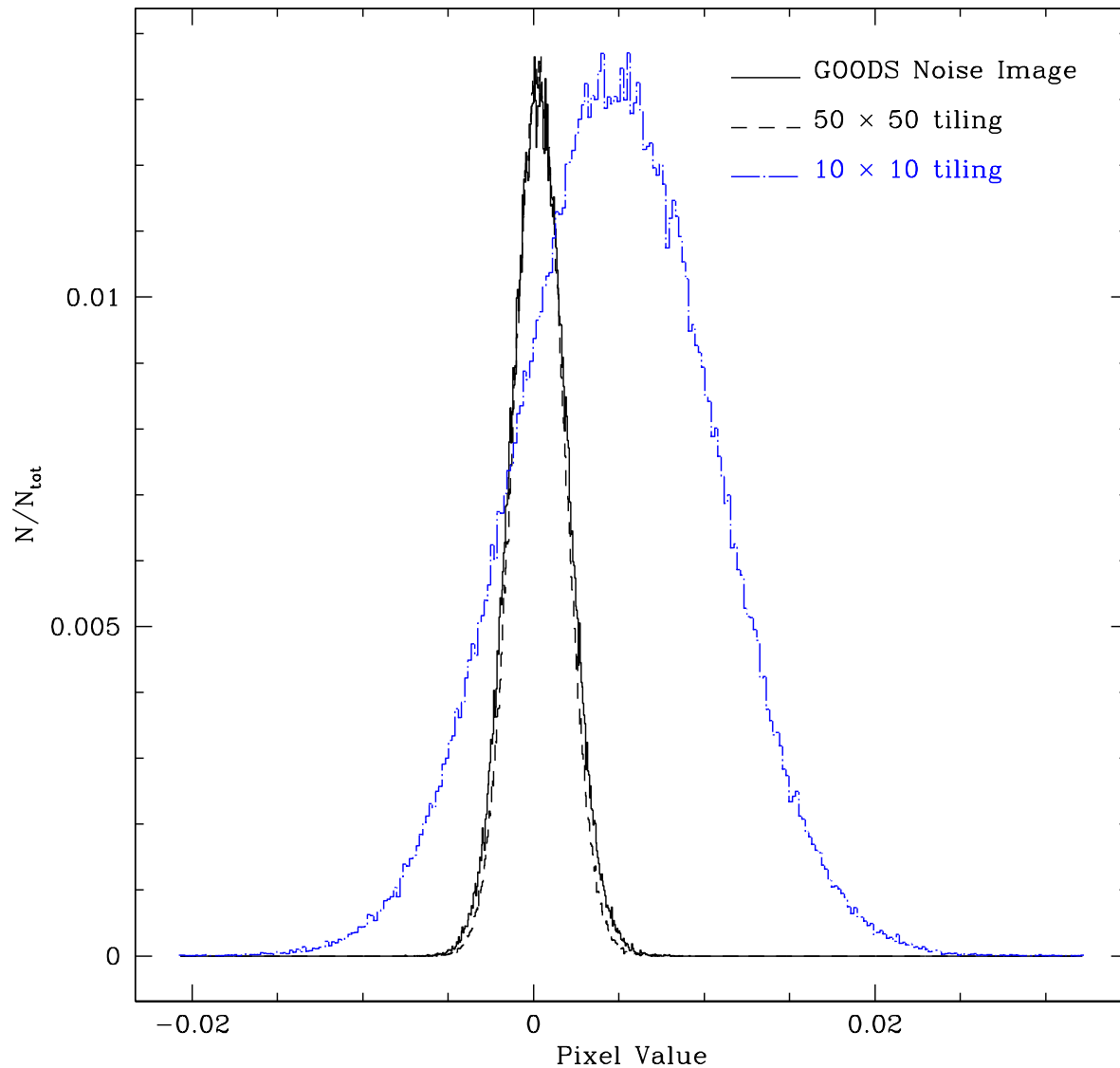


Fig. 1.— Histograms of pixel intensities for GOODS noise (solid), noise mosaics using a 50×50 -pixel sampling of the GOODS noise (dashed), and using a 10×10 -pixel sampling of the GOODS noise (blue, dot-dashed). The histogram for the mosaic using 10×10 -pixel tiles is significantly different from the intrinsic noise distribution. The distribution of pixel intensity of the 50×50 noise mosaic is nearly indistinguishable from that of the intrinsic GOODS noise distribution.

program uses a χ^2 minimization method to determine the best-fit parameters. We used the Sérsic profile, which models the light distribution of a galaxy as an exponential function with a variable half-light radius, r_e , and an exponential parameter, n , called the Sérsic index (Sérsic 1968). When n is fixed at a value of 1, the Sérsic profile is equivalent to an exponential disk; when $n = 4$, the Sérsic profile is equivalent to a de Vaucouleurs bulge. Each of our simulated galaxies was fitted twice: once using a single Sérsic function with a variable index, and once with two Sérsic functions with fixed $n = 4$ and $n = 1$ (bulge + disk). We also simultaneously fitted point-source (PS) components using the point-spread function (PSF) of the data, determination of which is based on GOODS field stars and is described in S08.

We developed a batch-fitting algorithm to fit AGN host galaxies in GALFIT (described in detail in S08), which we use here on our simulated galaxies. The batch-fitting algorithm uses a series of initial guesses to execute a first-pass fit of the central region of each AGN host galaxy, fitting the individual centroid positions of each component (Sérsic plus point source, or de Vaucouleurs bulge plus exponential disk plus point source). The second fit iteration zooms out to include the full extended galaxy and fits the central point-source magnitude and AGN host galaxy parameters (Sérsic index or bulge/disk decomposition, half-light radius, axial ratio, etc.). Finally, a third iteration is performed where all parameters are allowed to vary (except n in cases of a bulge + disk fit).

It is important to note that, while these simulations include thousands of AGN host galaxies, even the largest (current) galaxy surveys using ACS data provide no more than hundreds of AGN host galaxies that can be reasonably fitted with GALFIT. We can therefore (as in S08) follow up the batch fits by hand, using the results of the batch-mode fitting as initial guesses to further constrain the results for each AGN host galaxy. Due to the size of the simulated galaxy sample in this paper, we did not do this final hand-fitting step. Thus our conclusions about the fraction of cases for which accurate morphological parameters are recovered should be considered conservative when compared to a sample of galaxies whose fits are adjusted and verified individually.

3.2. Determination of Initial Parameter Guesses

For our real host galaxy sample, we use magnitude, flux radius, and position angle from the GOODS catalogs, which were created using SExtractor (Bertin & Arnouts 1996). Our simulated galaxies do not have a SExtractor catalog, but we simulated initial parameter guesses by introducing random errors into the true values.

Specifically, when determining initial guesses for parameters that can be measured from

a data image, we assume that the guess value is accurate to within the following: $\pm(2.0, 2.0)$ pixels in position, ± 0.5 in total magnitude, 10% in r_e and b/a , and 10° in position angle. We assumed no *a priori* knowledge of the Sérsic index n of each simulated galaxy, nor of whether each simulated galaxy was a two-component bulge plus disk system, or a system with either a pure bulge or disk. Our initial guess for the Sérsic index (or indices) of each fit is $n = 2.5$.

In the case of a multi-component fit, we assume that the total magnitude is split evenly among the components (i.e., that we have no prior knowledge of host:PS contrast ratio or bulge-to-total ratio), and we additionally assume that the measured position angle and axial ratio are the average of the actual values for each separate component after adding the random fluctuation to the sum.

3.3. Real Galaxies with Added Point Sources

In order to test whether we can recover central point sources from galaxies, we selected 450 *I*-band images of normal galaxies (i.e., not X-ray detected) from the GOODS-North and GOODS-South fields. The selection was performed so the sample has the same magnitude distribution as the full sample of galaxies in each of the GOODS fields, but was otherwise random. We assumed no knowledge of redshifts within the sample.

We fitted each of these galaxies with a single Sérsic profile in order to determine the baseline set of morphological parameters for each galaxy. These fit parameters (Sérsic n , magnitude, half-light radius r_e , etc.) were taken to be the “actual” galaxy parameters.

We then made nine copies of each galaxy, adding one point source to each, centered on the central pixel of the galaxy. The added point sources ranged in *I*-band magnitude from 21 to 29, in increments of 1 mag. This gave us a total of 4050 simulated AGN from the original 450 galaxies, with a large range of host galaxy-to-point-source contrast ratios, from $\sim 1000:1$ to $1:100$. These provide a straightforward means of assessing the effect of a central point source on the recovered parameters of a real galaxy.

Our convergence rate for the fitting routine depends on the magnitude of the added central point source. Of the models with $I_{PS} = 21$, 88% converge, whereas 64% of models with $I_{ps} = 29$ (significantly below the flux limit of our *I*-band sample) converged. This is due to the fitting program being unable to converge to a value for the central point-source magnitude. Examples of fit results for typical galaxies in our sample are shown in Figure 2.

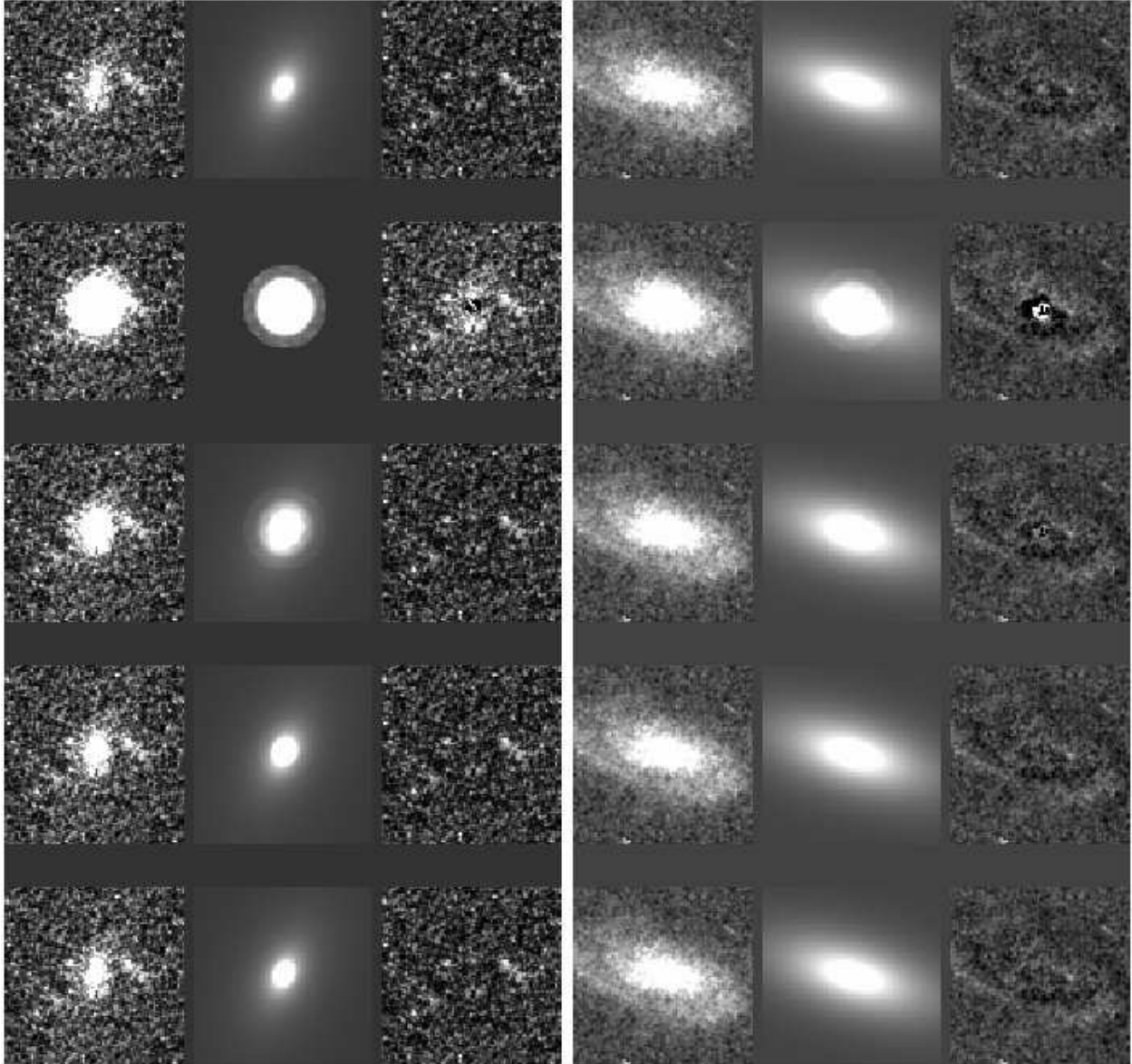


Fig. 2.— Example fit results for two AGN hosts simulated from real galaxies. For each galaxy, the top row shows the original GOODS galaxy (from left to right: galaxy, fit, residual). Each row below shows the host+fit+residual for added central point sources of magnitudes $I_{AB} = 22, 24, 26,$ and 28 , with the faintest point source in the bottom row. *Note:* These cutouts are zoomed-in to show the galaxies; the actual fitting regions are significantly larger.

3.4. Simulated Galaxies

The simulated hosts described in §3.3 provide information on how the presence of a central point source changes the fitted host galaxy parameters, but they do not allow us to explore redshift effects or quantify the absolute accuracy of the fit parameters. This can only be accomplished with a set of simulations for which we know the intrinsic properties of each simulated galaxy.

To that end, we simulated three kinds of galaxies with a range of parameters: pure de Vaucouleurs bulge (B) galaxies with fixed Sérsic $n = 4$, pure exponential disk (D) galaxies with $n = 1$, and composite galaxies with both bulge and disk (B+D) components in varying proportions. The galaxy parameters were chosen to be typical of bright, local galaxies (Binney & Merrifield 1998) and placed at $z = 0.125$. Redshifted samples were developed from these, as described below.

For the B and D type galaxies, the component parameters occupy a grid of four values for each parameter across the ranges $16.9 \leq I_{AB} \leq 20.4$ and $1.5 \leq r_e \leq 6.0$ kpc (for bulges); $4.0 \leq r_e \leq 10.0$ kpc (for disks), with axis ratios $0.25 \leq b/a \leq 1.0$. For the single-component fits, the position angle was fixed at 45.0° . This results in 64 B and 64 D galaxies, each of which is “inactive”, i.e., without a central point source. We create simulated AGN host galaxies by adding point sources to these. We used five values between $16.5 \leq I_{AB} \leq 24$ for the central point source, resulting in 320 B-type and 320 D-type AGN host galaxies, with contrast ratios ranging from $-1.3 \leq \log(L_{\text{host}}/L_{\text{PS}}) \leq 2.8$. Lastly, in order to ensure enough galaxies for statistical analysis after binning the fitted single-component sample, we made four copies of each B and D inactive galaxy and two copies of each B and D AGN host galaxy. This resulted in a total of 256 B and 256 D inactive single-component galaxies, and 640 B and 640 D AGN host galaxies.

For the B+D type galaxies, the parameter space includes more magnitudes so as to provide 20 input bulge-to-total ratios with $0.028 \leq (B/\text{Tot}) \leq 0.97$ [plus the single-component B and D fits, which have $(B/\text{Tot}) = 1$ and 0 , respectively]. In addition, the position angles of the individual components were allowed to vary such that some of the simulated B+D galaxies have components that are slightly ($\leq 15^\circ$) off-axis with respect to each other. The axis ratios between bulges and disks were also allowed to vary with respect to each other. These changes significantly increase the total number of double-component galaxies created; thus the number of radius, b/a , and point-source magnitude parameters used was decreased in order to keep the total number of galaxies from being prohibitively large from a computational perspective. This resulted in the creation of 2700 inactive double-component (B+D) galaxies, and 8100 B+D AGN host galaxies. Table 1 gives the parameter values used to create the entire local suite of 12,592 simulated single- and double-component galaxies.

Since we are also interested in distinguishing the effects of redshifting galaxies from the effects of evolving galaxies, the initial sample was defined to lie at $z = 0.125$, and three additional samples were placed at $z = 0.413, 0.738$, and 1.075 , corresponding to the redshifts at which the centers of each of our GOODS filters (F435W, F606W, F775W, and F850LP) are in the rest-frame B (F435W) band.

To redshift each galaxy, we used a concordance cosmology with $\Omega_{tot} = 1$, $\Omega_{\Lambda} = 0.73$, and $H_0 = 71 \text{ km s}^{-1} \text{ Mpc}^{-1}$ (Spergel et al. 2003) to calculate the cosmological dimming and loss of resolution corresponding to each redshift. Because the size of the ACS PSF does not change with redshift, we assume that the size of AGN central point sources will also stay fixed with redshift, unlike the host galaxy. We therefore created the redshifted AGN by redshifting the model host galaxy (in flux and size) separately from the central point source (in flux only) and adding them together before convolving with the ACS PSF and adding noise to the image. The redshifting of each of the 12,592 galaxies produced another 12,592 galaxies at each final redshift, for a total of 50,368 fully simulated galaxies located at four different redshifts from $0.125 < z < 1.075$.

We fit each using our batch-fitting algorithm. Each galaxy was fit twice: once with a generalized Sérsic profile plus a point-source component, and once with a combination of de Vaucouleurs bulge, exponential disk, and point source. Inactive galaxies were also fit without point-source components. Examples of fit results for typical galaxies in our sample are shown in Figure 3.

4. Results And Discussion

4.1. Existing Galaxies with Added Point Sources

We are interested mainly in three properties of these models: how well they recover the input point-source magnitude, how well they recover the baseline host galaxy parameters, and how the accuracy of the host galaxy parameters relates to the point-source magnitude and/or the contrast ratio between central point source and host galaxy.

4.1.1. AGN (Point Source) Recovery

Figure 4 shows the degree of recovery of the central point-source magnitude for input point sources. As expected, brighter point sources are more accurately recovered. At all

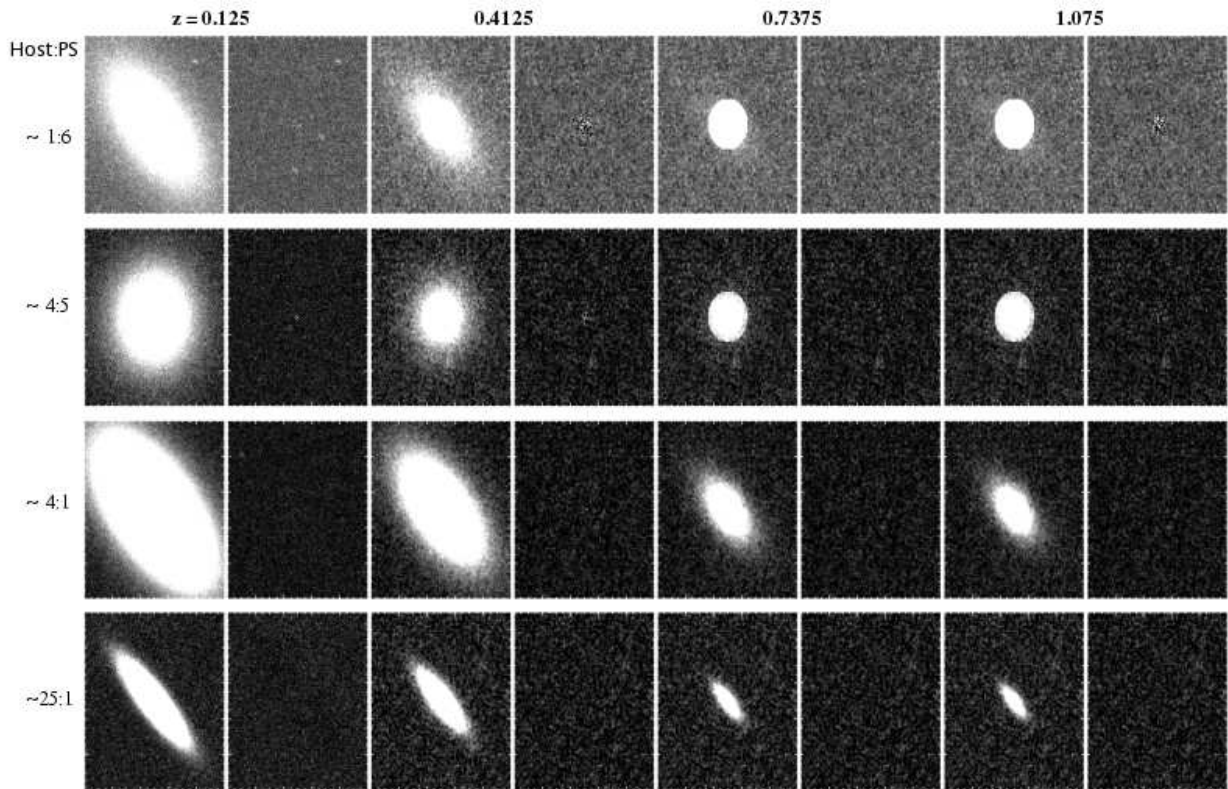


Fig. 3.— Example fit results for four fully simulated galaxies at four different redshifts. Each row shows one galaxy. The first two columns show the image of the galaxy at $z = 0.125$ and residual. Each successive pair of columns from left to right shows galaxy and residual for $z = 0.4125, 0.7375$, and 1.075 , respectively. *Note:* These cutouts are zoomed-in to show the galaxies; the actual fitting regions are significantly larger.

values of input point-source magnitude, the fitted value of the point-source magnitude tends to either converge to the true input magnitude *or* remain at the input guess magnitude.

In all cases, we can easily separate these two groups with a simple reduced χ^2_ν cut ($\chi^2_\nu < 2.0$). After the cut, the number of remaining poor fits is very low, as is the number of good fits removed by the cut: both are less than 5%, even in the limiting cases of very high and very low input point-source magnitude. This level of contamination/excess removal of good fits is not strongly dependent on the value at which we choose to cut χ^2 , nor is it strongly dependent on the input point-source magnitude.

The rms uncertainties of the recovered point-source magnitudes for each input point-source value are shown in Table 2. These values reflect the systematic uncertainties in the fitted parameters, and should be added to the statistical error in fitted point-source magnitude returned by GALFIT.

4.1.2. Host Galaxy Parameter Recovery

Figure 5 shows the correlation between the fitted model’s host galaxy magnitude and the actual host magnitude (as determined before the addition of the central point source). The percent completeness of the low-error sample compared to the full sample varies greatly across a range of contrast ratios between host galaxy and central point source. For very faint central point sources, the host galaxy magnitude is very well recovered, whereas for very bright point sources the fraction of host galaxies with well-recovered parameters is very low ($\sim 15\%$).

Our simulations show that the reduced χ^2_ν parameter is generally not sufficient to distinguish good from poor host galaxy fits. If we also limit the relative error of the effective radius parameter, however, the fraction of selected galaxies that recover the true magnitude of the host galaxy improves significantly. With the combination of χ^2_ν and σ_{r_e}/r_e parameters, we remove more than 85% of the fits with magnitude differences of 0.5 dex or more from the actual galaxy magnitudes. The number of well-fitted galaxies that are also removed from the sample ranges from 5% to 20%, depending primarily on how conservatively we choose our relative σ_{r_e} cut. Figure 5 reflects a cutoff value of $(\sigma_{r_e}/r_e) = 0.8$, which removes 88% of poor fits and 12% of the good fits from the $I_{\text{PS}} = 24$ sample.

Figure 6 shows how well we recover the Sérsic index, n . The same error cuts (χ^2_ν and σ_{r_e}/r_e) efficiently reject the inaccurate fits. The fraction of models whose fitted n values deviate by more than $\Delta n = 2$ compared to the n values of the unaltered galaxies increases significantly with increasing point-source flux. That is, a very bright central point source

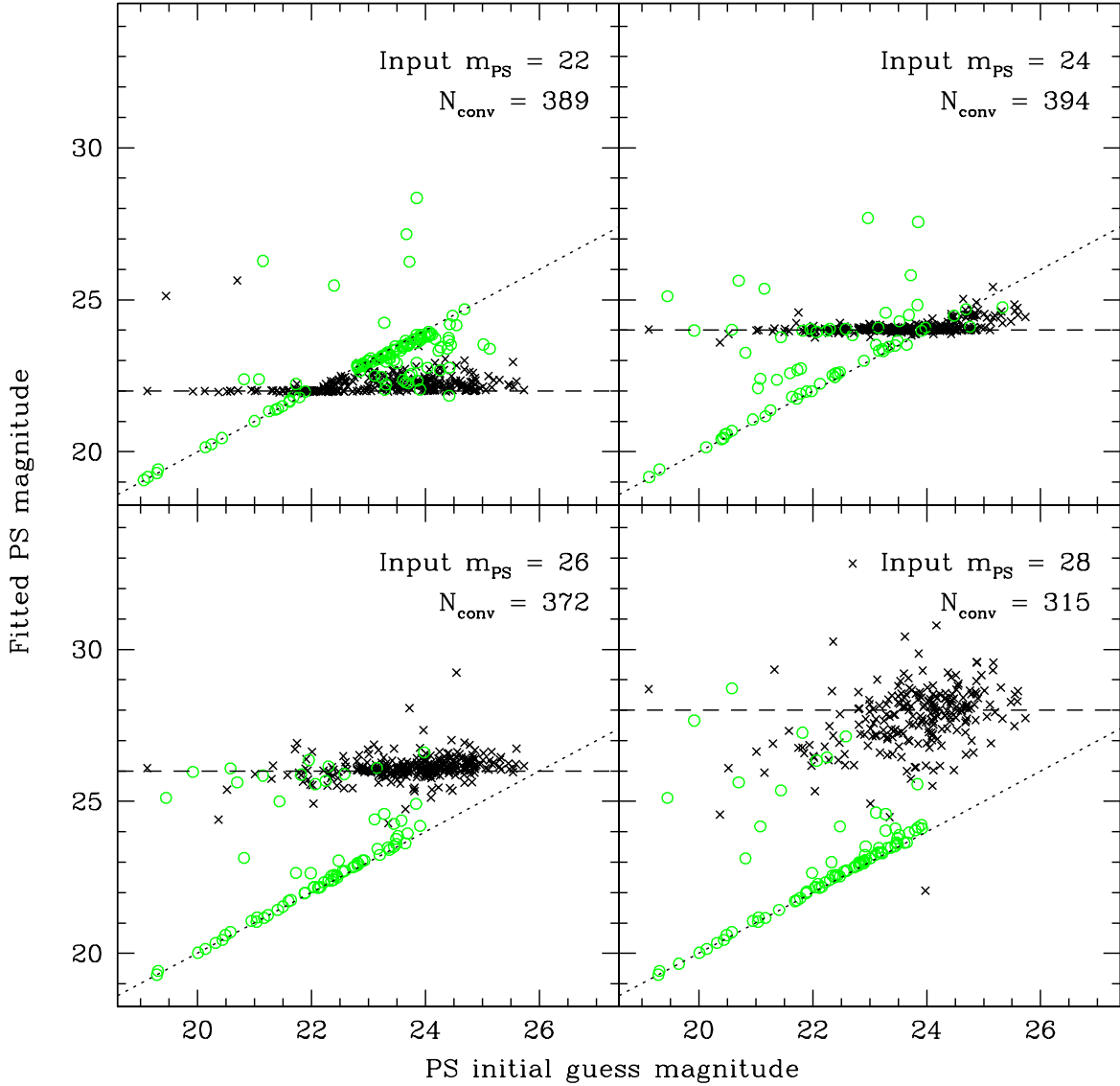


Fig. 4.— Recovery of magnitude of a point source added to real galaxy images, for: input point-source magnitudes of 22, 24, 26, and 28 mag. The fitting recovers the point-source magnitude nicely after making a simple $\chi^2_\nu < 2.0$ cut (black crosses), with a larger spread for fainter values of the input point source, as expected. Fits with a large value of χ^2_ν are shown as green open circles; N_{conv} indicates the number of fits (out of 450) that converged automatically for this input point-source magnitude. The dashed horizontal line shows $m_{\text{out}} = m_{\text{in}}$, so fits falling on this line perfectly recover the actual point-source magnitude. The dotted line shows $m_{\text{out}} = m_{\text{guess}}$: fits on this line converged to their initial guess point-source magnitude, and the final fitted magnitude is wrong; nearly all of these fits are removed by the χ^2_ν cut.

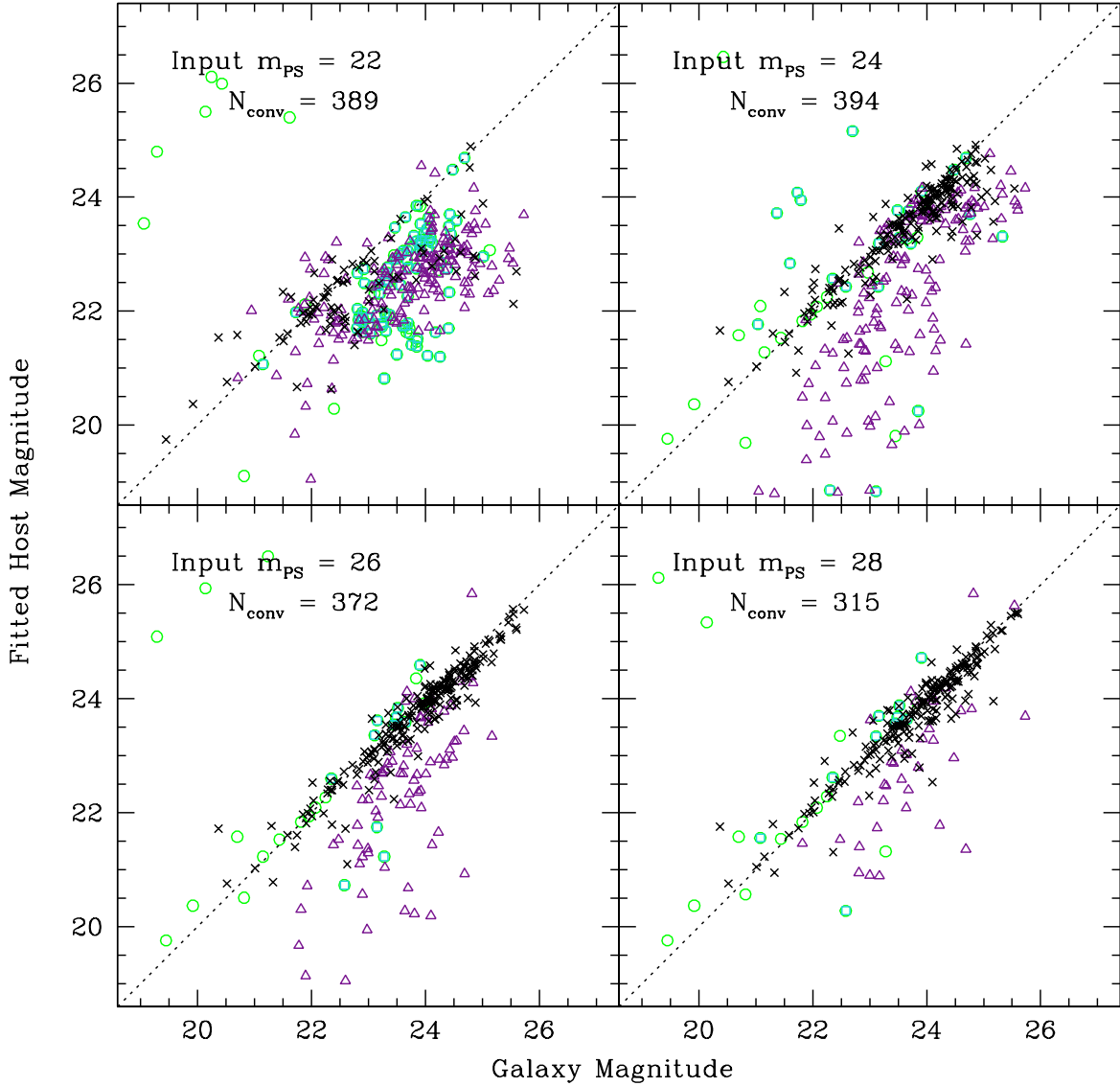


Fig. 5.— Fitted host galaxy magnitude versus actual galaxy magnitude for fits to actual galaxies with added point sources. Excluding high χ^2_{ν} values and effective radii with large fractional errors ensures a high fraction of good fits, with moderate uncertainties. Green open circles indicate fits with high χ^2_{ν} values. Cyan open squares indicate fits with excessive errors on the effective radius fit parameter ($\sigma_{r_e} \geq 0.8 \times r_e$). Purple open triangles represent fits with both high χ^2_{ν} and high σ_{r_e} . The dotted line represents equal input and recovered magnitudes (i.e., perfect recovery). The error cut removes some of the fits that do lie on the 1:1 line, regardless of the precise value for the σ_{r_e} cut.

can easily be confused with a concentrated (high- n) Sérsic value. For all values of the added point-source magnitude, however, the same combination of χ_ν^2 and relative r_e error is sufficient to remove 88% of the inaccurate fits from the data, while removing less than 15% of the well-fitted models.

4.1.3. Dependence of Parameters on Host:AGN Contrast Ratio

Figure 7 shows the relation of fitted host galaxy parameters to the contrast ratio between the host galaxy and the added central point source, for the 1491 (of 4050) sources that are not eliminated by the combination of χ_ν^2 and σ_{r_e}/r_e cuts. These include galaxies with all possible values of input point-source magnitude.

The left panel of Figure 7 shows the difference between the fitted host galaxy magnitude and original galaxy magnitude for the PS-added models. The recovered magnitudes are no different on average than the correct parameters. For galaxies with contrast ratios of at least $\log(L_{\text{host}}/L_{\text{PS}}) < -0.6$, the host galaxy magnitude is well recovered, such that a weighted least-squares fit to those data with contrast ratios ($L_{\text{host}}/L_{\text{PS}}$) greater than 1:4 has a slope within 1% of zero, indicating no correlation between contrast ratio and recovered host galaxy magnitude. The scatter in the plot indicates that, while the sample as a whole is well-recovered, individual galaxies may have large differences in recovered parameters due to the presence of a point source. We see this result again in the right panel, which shows the difference between fitted and original Sérsic index as a function of host-to-PS contrast ratio. The inaccuracy in Sérsic index is larger when the added central point source is more than 4 times as bright as the host galaxy: the slope of the weighted least-squares fit is 6% for ΔI_{AB} and 11% for Δn . With proper error cuts, and for galaxies brighter than 1/4 of the point-source magnitude, our host galaxy fits are not significantly contaminated by the central point source. However, the presence of a point source increases the uncertainty in fit parameters.

Figure 8 shows the median change in fitted parameters with input point-source magnitude. For very bright added point sources ($I_{AB} = 21$, $\langle \text{Host:PS} \rangle \approx 1 : 11$), all fit parameters deviate from their initially-determined values. The median Sérsic index is low by approximately $\Delta n = 1.75$, indicating that on average, galaxies with such bright point sources could be classified as disk-dominated even if they have more bulge-dominated intrinsic morphologies. The distribution is also very wide in the brightest-point-source bin: for such low host-to-PS contrast ratios, the Sérsic index is essentially completely uncertain. For fainter point-source magnitudes, recovery of the Sérsic index is far more reliable, although the uncertainty (indicated by the width of the distribution in each bin) is considerably larger than

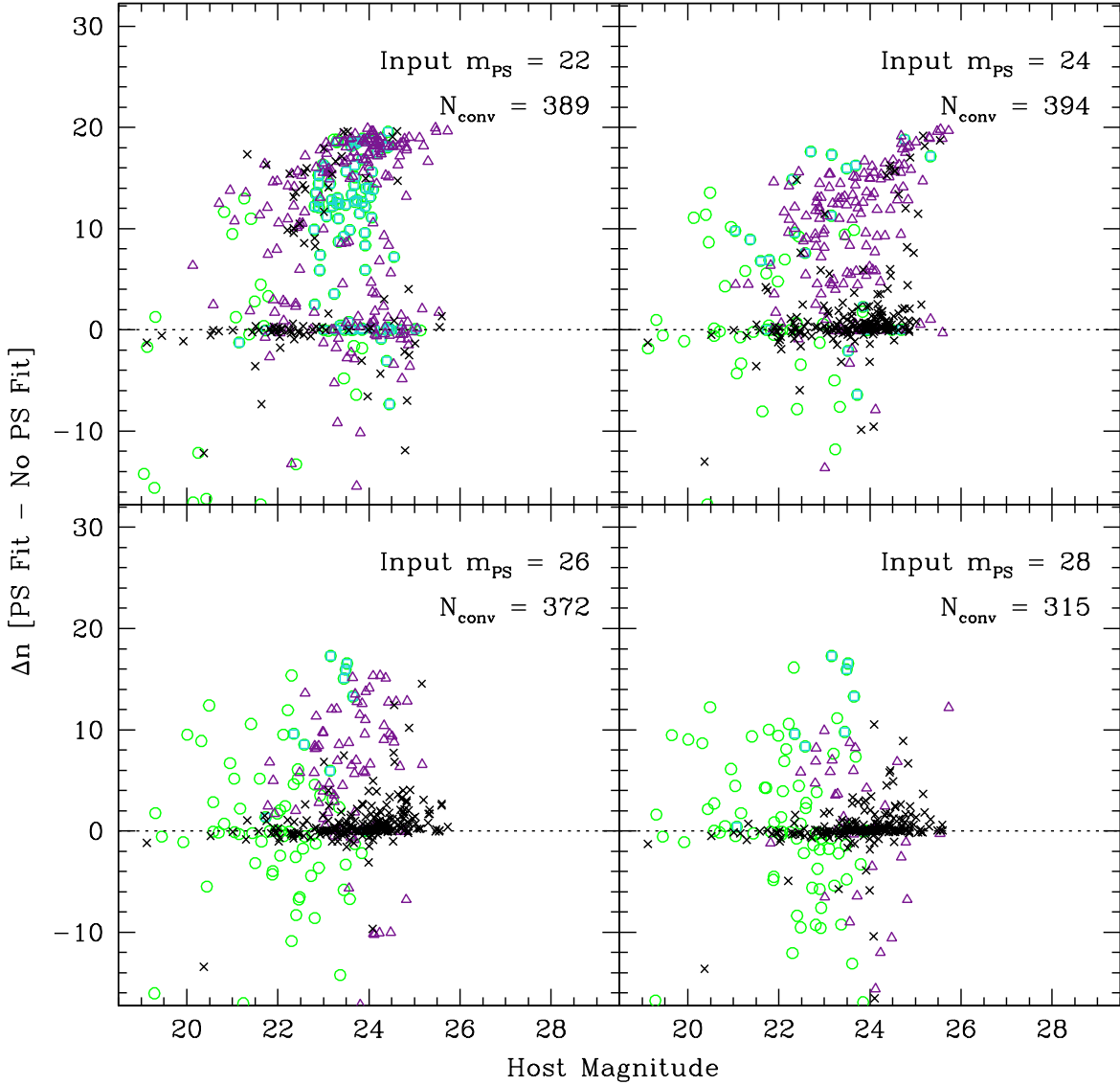


Fig. 6.— Change in Sérsic indices of host galaxies after adding point sources with original host magnitude. Excluding high χ_ν^2 and σ_{r_e}/r_e yields the correct Sérsic index (a proxy for morphological type). The color-coding of the points is the same as in Figure 5: green open circles for high χ_ν^2 , cyan open squares for high relative σ_{r_e} , and purple open triangles for both high χ_ν^2 and relative σ_{r_e} . The dotted lines at $\Delta n = 0$ indicate perfect recovery of the Sérsic index. As expected, the bright-point-source fits return mostly unreliable host galaxy parameters, in contrast to the faint-point-source fits, which return mostly reliable host galaxy parameters.

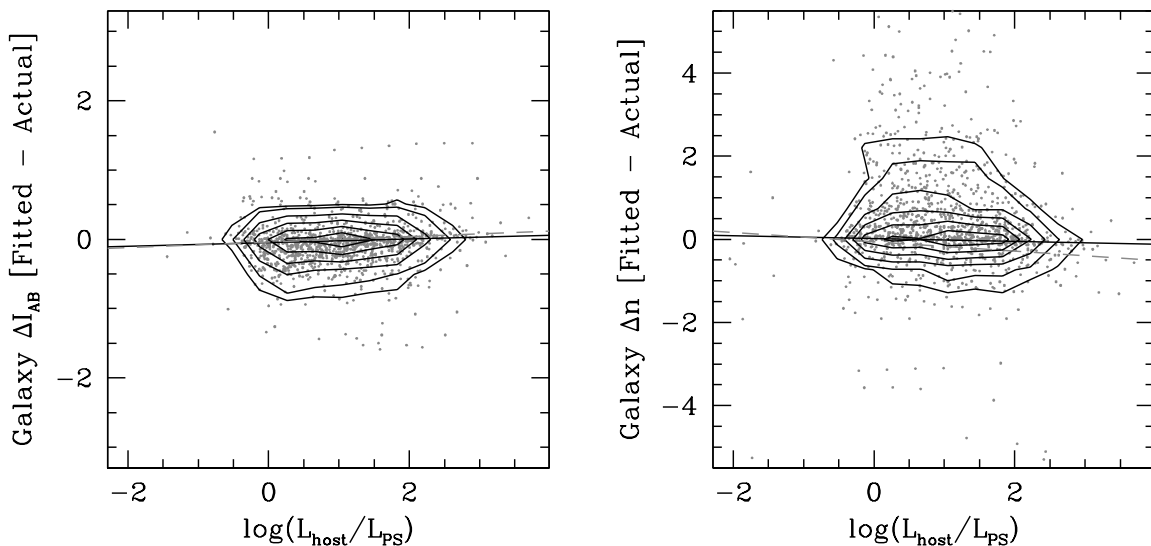


Fig. 7.— Accuracy of the host galaxy magnitude (left) and Sérsic index (right) as a function of the ratio of intrinsic galaxy luminosity to the added point-source luminosity. In both figures, contour plots are overlaid on the data points. Weighted least-squares fits to all data points (dashed lines) indicates that the recovery of galaxy magnitude and Sérsic index is very slightly correlated with host-to-PS contrast ratio. Excluding points with $\log(L_{\text{host}}/L_{\text{PS}}) < -0.6$, the weighted least-squares fit (solid lines) is consistent with zero slope (i.e., no correlation between Host-to-PS contrast ratio) for both plots.

that reported by the fitting routine.

The ratio of host and point-source luminosities is also incorrect at the brightest point-source magnitudes: in these situations the typical fitted point-source magnitude is very close to the input value, and the fitted host magnitude is too low (bright) by approximately 1.45 dex. Interestingly, the deviations in magnitude do not add to zero: because bright point-sources are also slightly too bright, the total magnitude is also underestimated (too bright) in the presence of a very bright central point source.

For point sources brighter than $I_{AB} = 24$, the distribution of recovered host galaxy magnitude is wide, such that the 68% confidence intervals span more than 1 dex in all bins. For those point sources with magnitudes fainter than 24 (which is approximately equal to the average magnitude of our initial galaxy sample), on the other hand, the model’s host galaxy magnitude is well recovered.

Since the faintest point-source magnitudes ($I_{AB} = 28, 29$) are below the 10σ point-source detection limit of our band, the fitted point-source magnitude for these cases is often at least 1 mag brighter than the input point-source magnitude, with 68% confidence intervals larger than 1 mag.

The Sérsic indices for the host galaxies are within $\Delta n = 0.25$ on average for most values of the added point-source magnitude. Since disks are generally more extended than bulges, the Sérsic parameter is lower (on average) when the central point source is so bright that the central portion of the host galaxy is dwarfed by the light in the wings of the central point source. In all but the brightest cases, however, the median difference between the model Sérsic index and the no-point-source index is smaller than the size of the morphological bins discussed for a typical AGN sample (e.g., Sánchez et al. (2004); Ballo et al. (2007), S08), so it is unlikely that a significant fraction has been mis-classified as disk-like or bulge-like due to the presence of a central point source.

The rms values of the recovered Sérsic indices and recovered host magnitudes for each input point-source magnitude are given in Table 2.

4.2. Fully Simulated Galaxies

4.2.1. Input Parameter Recovery

For our 12,592 fully simulated GOODS galaxies, we apply the error cut determined above, using a combination of χ^2_ν and σ_{r_e}/r_e to distinguish good fits from poor fits. Within the single component galaxies, this error cut results in 706 of 896 B type galaxies with “good”

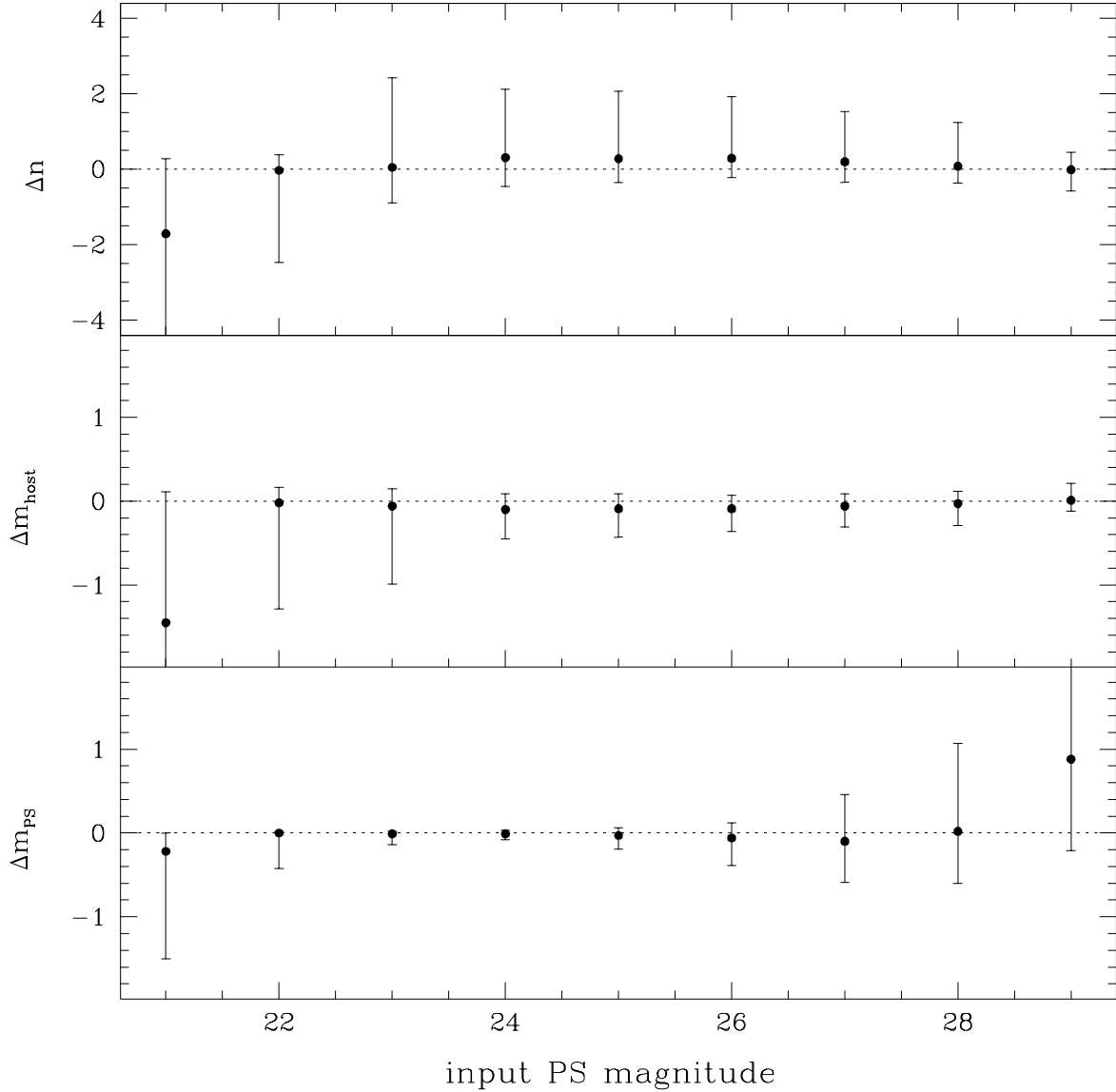


Fig. 8.— Median change in Sérsic index n (upper), host magnitude (middle), and point-source magnitude (lower) versus input point-source magnitude. Each point represents the median value of all the galaxies with the given input point-source magnitude whose fits pass the χ^2_ν and σ_{r_e}/r_e cut described in the text. The host Sérsic indices (top panel) are generally well-recovered for all but the brightest input point sources. The host magnitudes (middle panel) are also well-recovered in all but the brightest input point-source bin, with the error bars (representing the width of the distribution encompassing 68% of sources) increasing with increasing point-source strength. Point-source magnitudes (bottom panel) are recovered well until the input magnitude is fainter than the published 10σ point-source detection limit of the data.

fits and 708 of 896 D type galaxies with “good” fits.

The recovery of the Sérsic index for both of these types of galaxy models is shown for the $z = 0.125$ sample in Figure 9. If we classify galaxies as bulge-dominated when their fitted $n > 2.0$ and disk-dominated when their fitted $n < 2.0$, the level of misclassification based on these simulations is less than 15% for AGN host disk galaxies and less than 10% for AGN host bulge galaxies. Fewer than 10% of inactive disks are misclassified as bulges using the above cut; no inactive bulges are misclassified as disks. For any local sample of single-component galaxies (the simplest possible case), then, the Sérsic parameter is a very reliable indicator of morphological type.

The recovery of the $z = 0.125$ sample of two-component (B+D) galaxies is shown in Figure 10. The fitted bulge-to-total light ratio, $B/Tot = L_B / (L_B + L_D)$, is within $|\Delta(B/Tot)| \leq 0.15$ for 50% of our AGN host sample and 66% of our inactive sample. A Gaussian fit to the data in Figure 10 gives an estimate of uncertainty in the bulge-to-total parameter of $\sigma_{B/Tot} = 0.04$. However, the contamination from very deviant fits (i.e., the wings of the histogram in Figure 10) is large. Approximately 14% and 13% of host and inactive galaxies remaining in the sample after our error cut have $\Delta(B/Tot) < -0.15$, and 36% of host galaxies and 21% of inactive galaxies have $\Delta(B/Tot) > 0.15$.

Figure 11 shows the ratio of fitted-to-input bulge-to-total flux ratio as a function of the intrinsic contrast ratio between the host galaxy and the central point source. The median and 1σ error bars (defined here as the values encompassing 68% of the points in each bin) for the distribution of simulated galaxies without central point sources are plotted for comparison at a value of $L_{host}/L_{PS} = 3$. In general, the presence of a central point source skews the fits to slightly high values of the bulge-to-total ratio. For galaxies where the central point source is very bright, the spread is higher, such that a galaxy may fit to a bulge-to-total ratio twice the intrinsic value and still be within 1σ of the median value. Based on this, one could attempt to correct the bulge-to-total ratio for the presence of a central point source, but a bulge-to-total ratio fitted to a host galaxy could be overestimated by as much as 100%.

This large tail of high fitted bulge-to-total values has several causes. The radius of the bulge may converge to an unphysically high value; this causes the luminosity bulge-to-total ratio to skew high. This appears to be slightly more common when the intrinsic luminosity of the galaxy is disk-dominated, i.e., with $(B/Tot) \leq 0.3$. In addition, if the total source magnitude is not well-conserved during the fit, the bulge-to-total ratio typically deviates from the input value by at least 10% (high or low). This is more likely to occur when the bulge and disk components have approximately equal luminosity, or the bulge is slightly brighter [$0.45 \leq (B/Tot) \leq 0.7$].

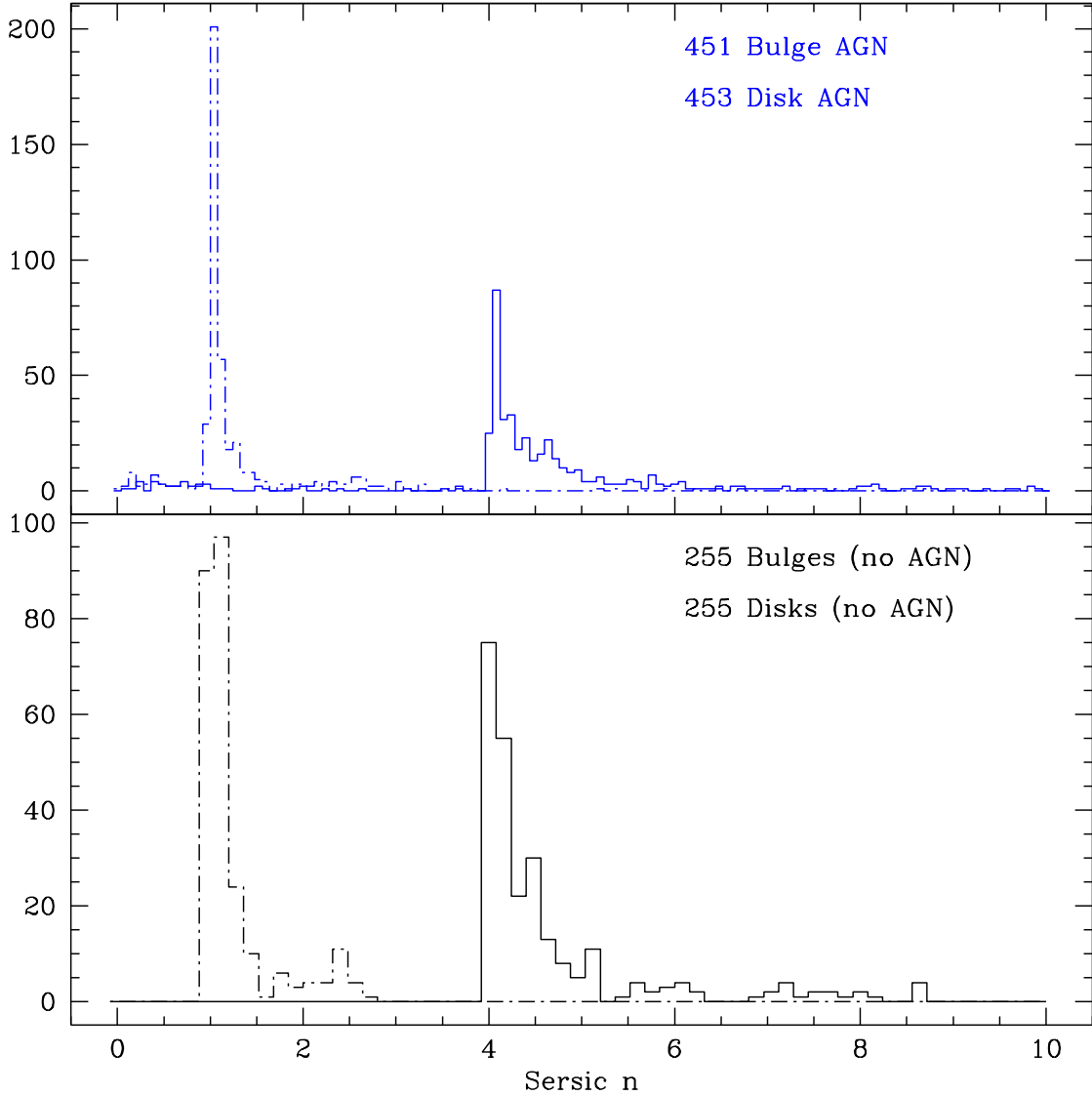


Fig. 9.— Recovery of Sérsic index n for the single-Sérsic fits to simulated single-component B and D AGN host galaxies (blue, top) and inactive galaxies (black, bottom). For the bulge-dominated B galaxies (solid histograms), the average fitted Sérsic index is slightly higher than the input $n = 4$ in both AGN and inactive galaxies; however, these are unambiguously classified as bulge-dominated galaxies, with fewer than 10% of bulge host galaxies misclassified as disk-dominated galaxies and no bulge inactive galaxies misclassified as disks. For the disk-dominated D galaxies (dot-dash histogram), the recovery of the input $n = 1$ is also excellent, with 13% of D host galaxies and 9% of D inactive galaxies having $n > 2.0$. The separation between the typical fitted n for B and D galaxies is robust and indicates that we can use the Sérsic index as a strong indicator of galaxy morphology for single-component local galaxies with and without central point sources.

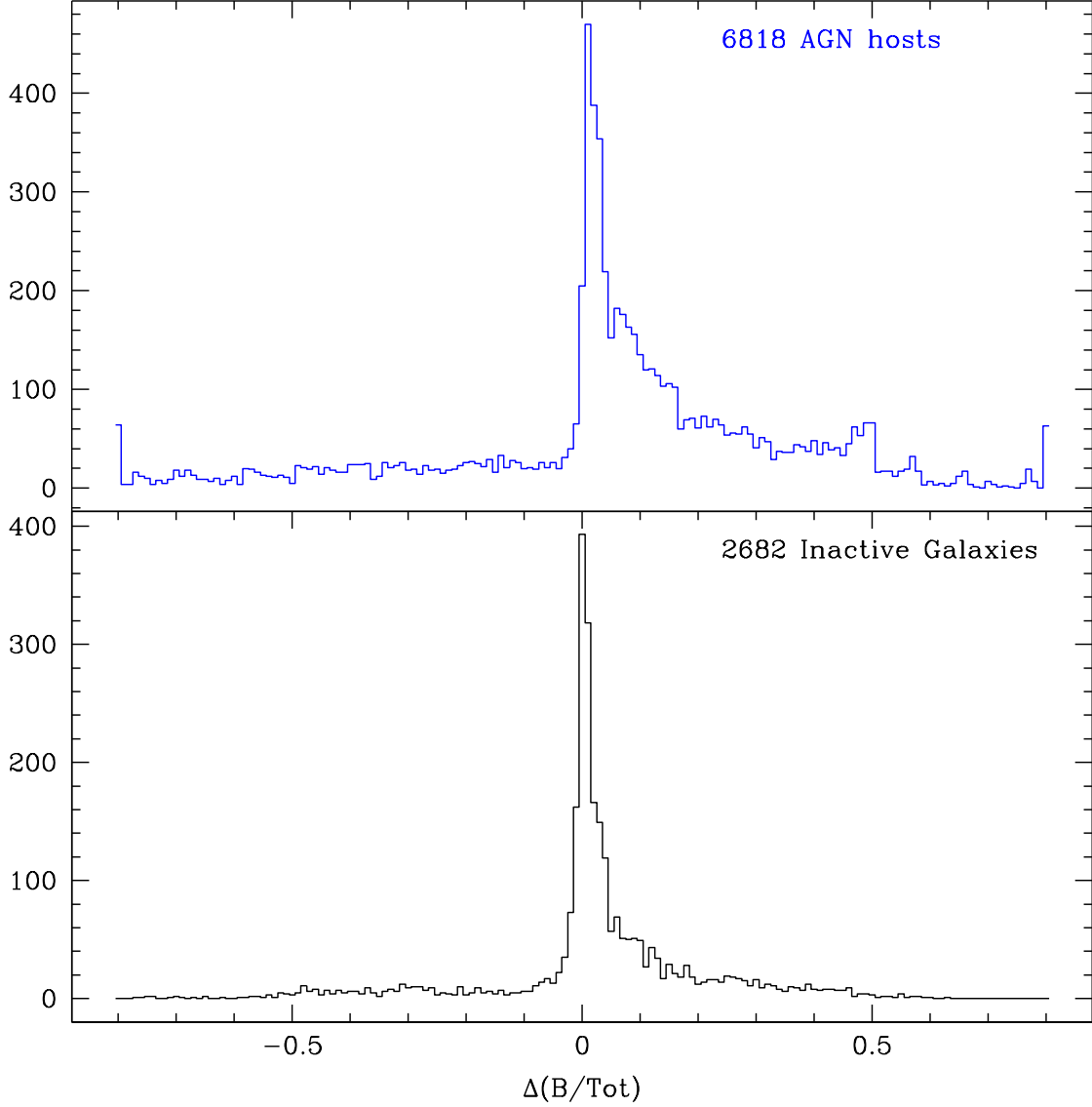


Fig. 10.— Recovery of input bulge-to-total ratio for the fully-simulated two-component galaxies. We define $\Delta(B/Tot) > 0$ to mean the fit was more bulge-like than the input galaxy. A Gaussian fit to the Host galaxy distribution gives $\sigma_{BT} = 0.04$, but there is a large asymmetric tail on each distribution indicating that the samples are skewed toward more bulge-like fits than the intrinsic distribution. 36% of host galaxies and 21% of inactive galaxies have $\Delta(B/Tot) > 0.15$.

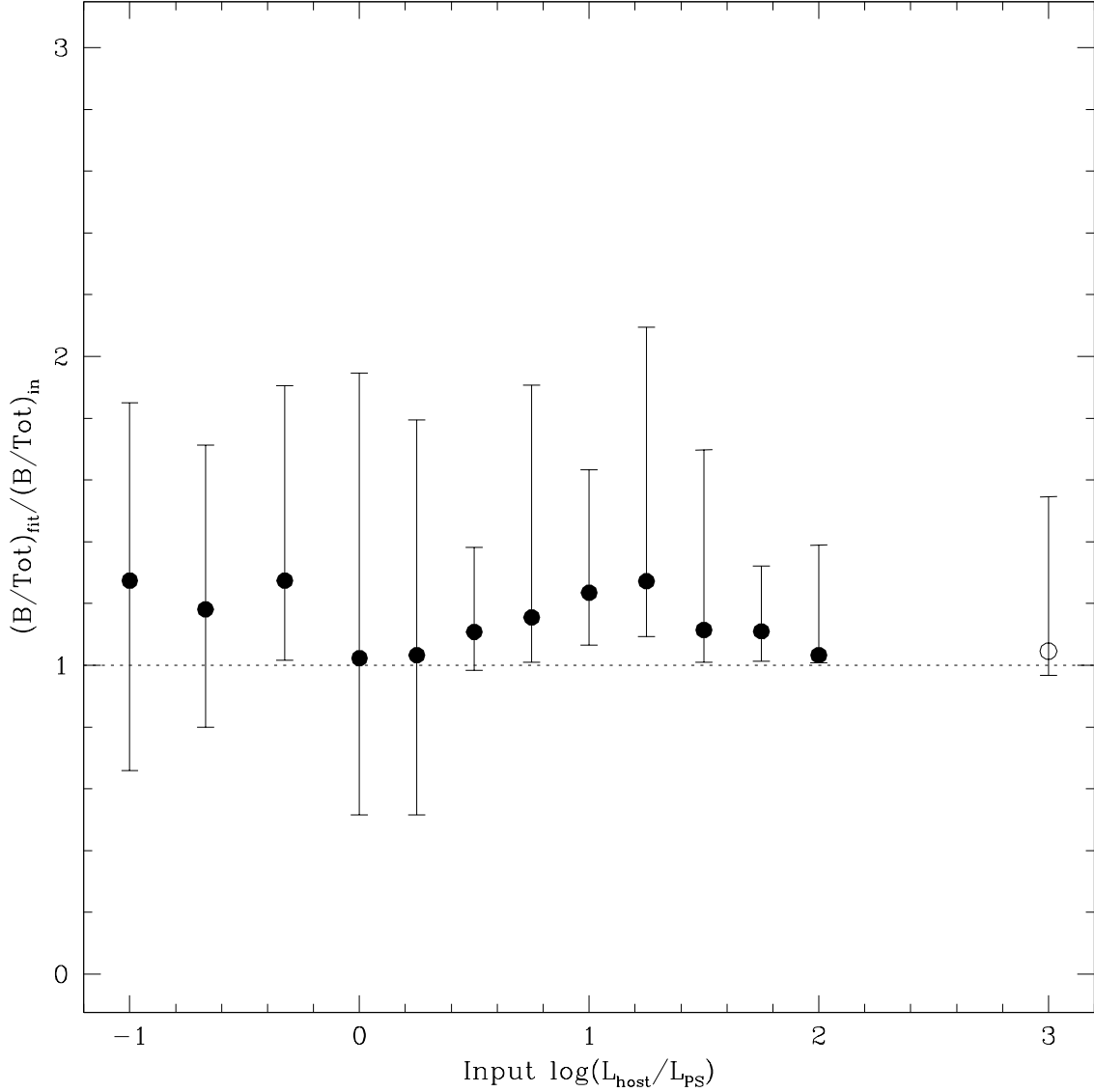


Fig. 11.— Ratio of fitted-to-input bulge-to-total vs. input host-to-PS contrast ratio. Points plotted are the median values in each bin, with error bars marking the range of values containing the central 68% of the points in each bin. The open circle shows simulated galaxies with no added point source; this bin recovers input bulge-to-total ratio closely, with a tail of high bulge-to-total values. For simulated host galaxies, the recovered bulge-to-total ratio is generally high by 10-20%, and the distribution of points in each bin is wider for galaxies where the central point source is at least as bright as the host galaxy.

About 18% of the two-component AGN host fits result in either a bulge or disk half-light radius that is unphysically low given the input sizes of both in our sample. These fits span the entire range of Δ (B/Tot) values, and are far more common when the central point source is intrinsically bright. For the locally-defined sample, 79% of B+D bulge components and 63% of B+D disk components with fitted $r_e < 5.0$ pixels are those with the brightest central point source; this comprises 26% of all two-component sources with the brightest central point source. It is worth noting that these fits typically show residuals that clearly indicate a poor fit, and they can therefore be removed from the well-fitted sample on visual inspection, or followed up with individual fitting to improve the fit.

The recovery of bulge and disk sizes in our sample is shown in Figure 12. The distribution of Δr_e for single-component galaxies (pure bulges and disks) is sharply peaked at a value of $\Delta r \approx 0$ (in pixels). A total of 66% of pure bulges and 65% of pure disks recover their input radii within $-1 \leq \Delta r_e \leq 12$ pixels. The discrete peaks at negative Δr_e represent those fits that converged to unphysically low values ($r_e < 5.0$ pixels for the local sample). Less than 5% of single-component fits converged to extremely large radii ($\Delta r_e > 150$ pixels).

The radius parameter converges to extremely high values far more frequently for the two-component fits, and with higher frequency for the bulge components of two-component galaxies (20%, B+D bulges) than for the disk components of two-component galaxies (13%, B+D disks). The high- Δr_e tail for B+D bulges is a result of confusion with the central point source of the simulated AGN host. Not only are bulges more compact than disks within our B+D galaxies (and typically within real galaxies as well), but the slope of their light profile more closely resembles the light profile of the ACS PSF than does an exponential disk profile. This can lead to uncertain bulge radii and magnitudes, especially when the intrinsic luminosity of the bulge is similar to that of the central point source. Disk components of B+D galaxies are not as readily confused with the central point source: their fit typically fails when the surface brightness of the disk component is too low compared to the bulge and point source components.

Figure 13 demonstrates a possible method of separating good from poor two-component fits. After removing those fits where either the bulge or disk converged to $r_e < 5.0$ pixels, additionally requiring that the total source magnitude be conserved to within $|\Delta m_{tot}| < 0.5$ (determined by comparing the fitted total source magnitude with a measured, aperture-corrected magnitude), and/or that the flux-weighted effective radius of the fit be no more than 90 pixels larger than the measured half-light source radius¹ removes 81% of sources with $|\Delta$ (B/Tot) > 0.15 and retains 83% of sources within 0.15 of the input bulge-to-total

¹This value was chosen because it is twice the observed radius of the largest source in our sample.

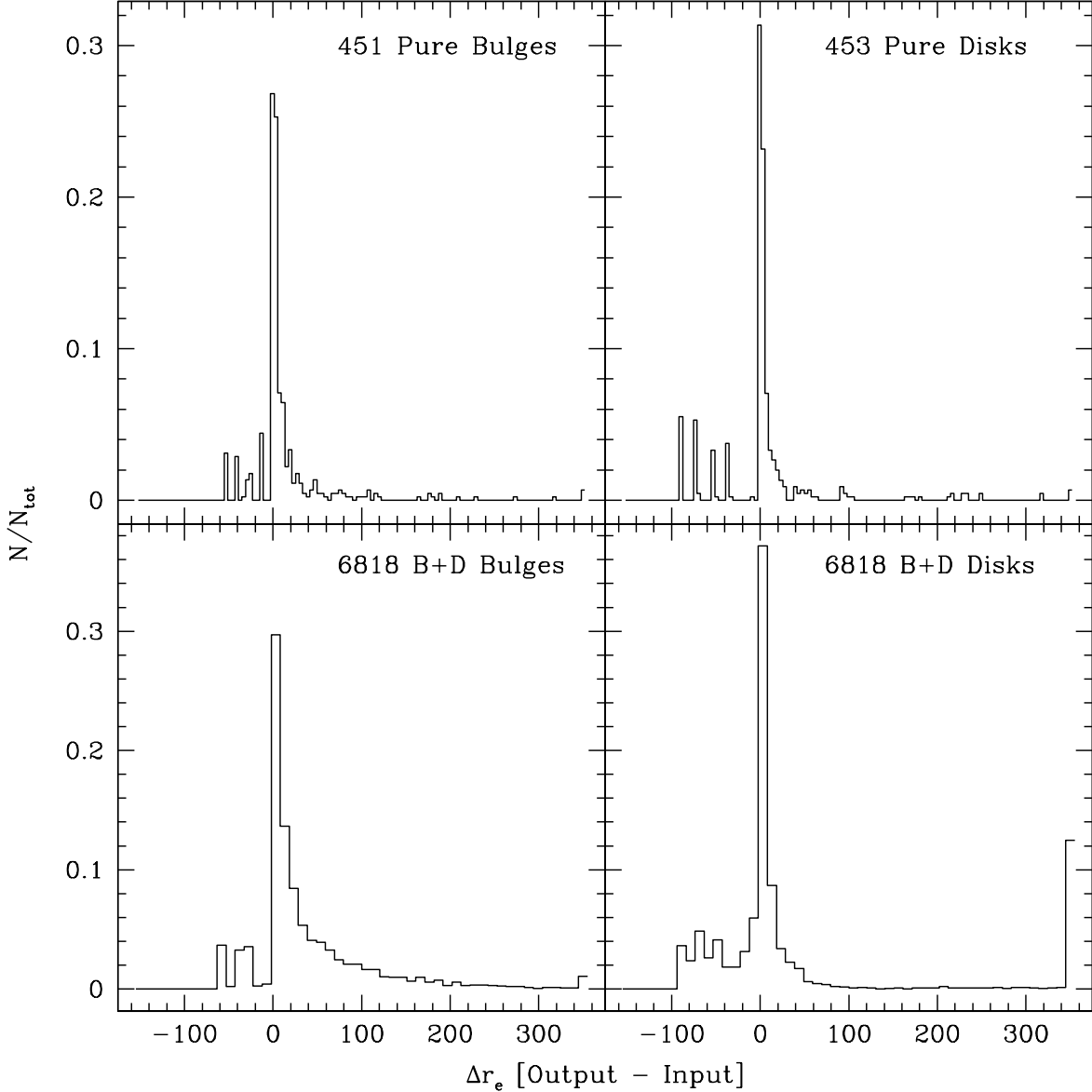


Fig. 12.— Histograms of the change in half-light radius for pure bulge (top left), pure disk (top right), B+D bulge (bottom left) and B+D disk (bottom right) fits to simulated AGN hosts. The majority of fits converge to a value that is equal to or greater than the input value of the half-light radius for that source or source component. The small discrete peaks at negative Δr_e values are comprised mostly of fits for which r_e converged to an unphysical value for our sample, $r_e < 5$ pixels. Single-Sérsic fits typically recover the sizes of pure bulges and pure disks with about the same level of success. However, the local sample of two-component galaxies indicates that bulge component radii are more likely to converge to a value that is at least 50 pixels too high, or at least twice the intrinsic radius. Local disk components are more likely to be underestimated, with a lower σ for the high- Δr_e distribution than for B+D bulges.

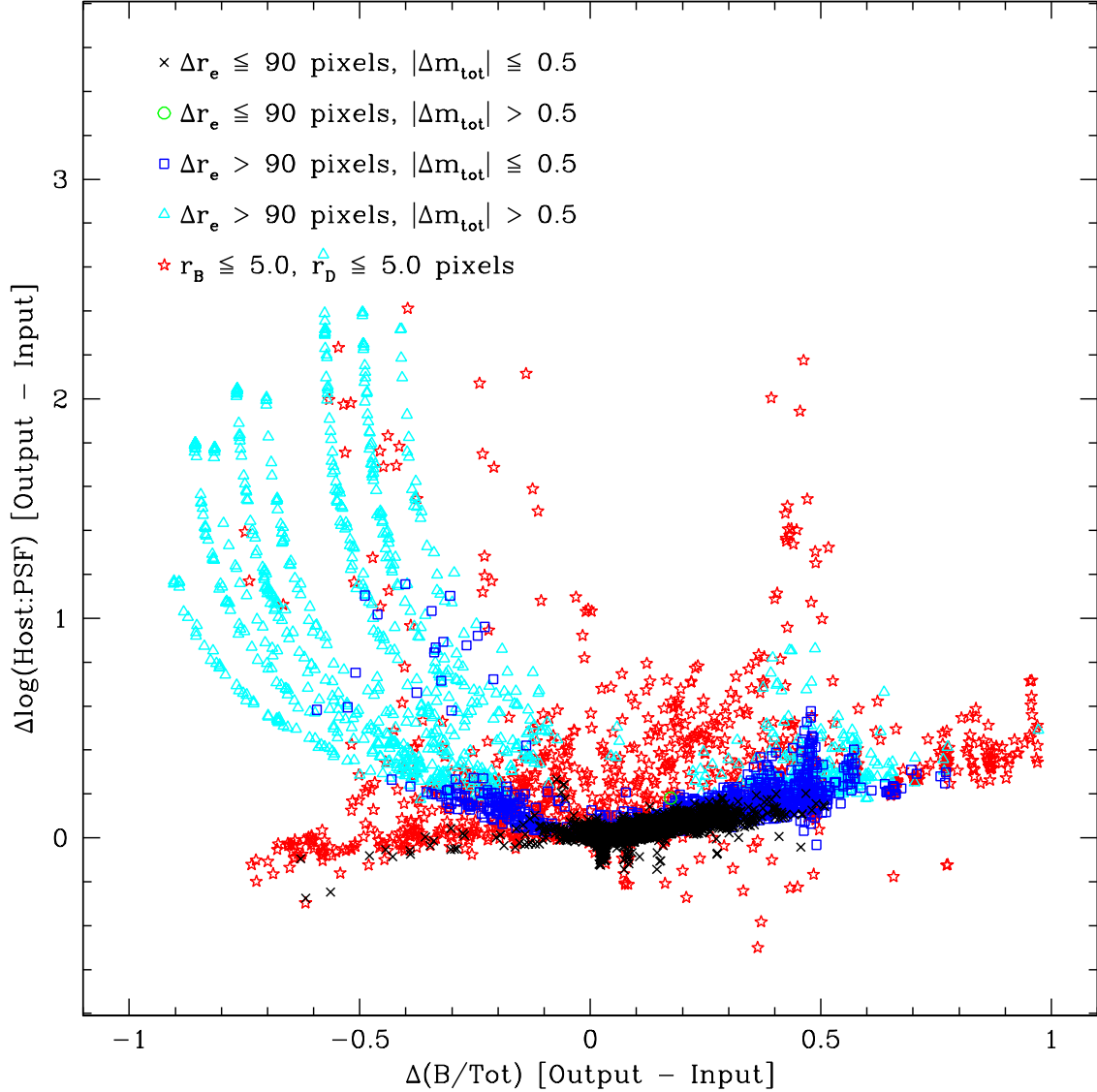


Fig. 13.— Deviation from input host-to-PS contrast ratio versus deviation in bulge-to-total ratio. Fits located at $(0, 0)$ perfectly recovered the input bulge-to-total ratio and the Galaxy-AGN luminosity ratio ($L_{\text{host}}/L_{\text{PS}}$). Requiring that the difference between the half-light radii of the host be no more than 90 pixels larger than that observed for the entire source ($\Delta r_e \leq 90$), that the total source magnitude luminosity be conserved to better than $|\Delta m_{\text{tot}}| \leq 0.5$ mag, and that the radii of neither the bulge nor the disk component be less than 5 pixels (typically indicative of a poor fit) cuts 81% of sources with $|\Delta(B/\text{Tot})| > 0.15$, and retains 83% of sources with $|\Delta(B/\text{Tot})| \leq 0.15$.

ratio. This also constrains the fitted host-to-PS contrast ratio to within 8% of the input value for 95% of the remaining “good” sample. However, this selection biases the remaining sample toward sources with faint central nuclei and preferentially retains bulge-dominated sources with intrinsic $(B/Tot) > 0.7$. In general, the result of two-component fits should be used with caution, even for a local, well-understood sample.

4.2.2. Detection of Central Point Sources

We established in §4.1.1 that central point sources can be recovered on average for a sample of simulated host galaxies created from the addition of a central point source to a real GOODS inactive galaxy, although the fraction of recovered point sources varies depending on the luminosity of the added point source. Using the χ^2_ν cut previously determined from this sample, we now examine the recovery of point sources with redshift and intrinsic morphological type. Figure 14 shows the fraction of fits in which the central point source was detected for our entire sample of fully simulated galaxies. In this case, our criteria for a “detected” point source is simple: the point source is considered undetected only if the magnitude parameter converged to a value considerably fainter than the detection limit of our simulated data ($m_{PS} = 27.1$ for our sample; Giavalisco et al. (2004)). Thus Figure 14 shows the fraction of fits for which any point-source magnitude was recovered, rather than those fits for which the magnitude is close to the intrinsic magnitude.

Figure 14 indicates that the point source is detected within the fit at least 90% of the time for all values of input $\log(L_{\text{host}}/L_{\text{PS}})$. The fraction is lowest when the point source and host galaxy have about equal luminosity. The detection fraction increases to more than 95% at the highest values of input $\log(L_{\text{host}}/L_{\text{PS}})$, even for cases in which the point source is 100 times fainter than its host galaxy. This is due to the fact that the convergence fraction is lower for these bins; fits where the central point source may not have been detected are less likely to converge, driving the detection fraction higher for those fits that did converge.

While we are primarily interested in the recovery of host galaxy parameters and optical detection of central AGNs, we also want to characterize the fraction of spurious optical point-source identifications. Thus, Figure 15 shows the results of a Sérsic + PS fit to *inactive* galaxies with no intrinsic central point source. We find a significant difference in the number of false point-source detections between pure disk and pure bulge galaxies. Only $\sim 1\%$ of pure disk inactive galaxies detect² a central point source when none are present. However, we

²We define “detected” as having been fit with a magnitude brighter than the published 10σ point-source detection limit of the GOODS survey (from which we take our noise properties).

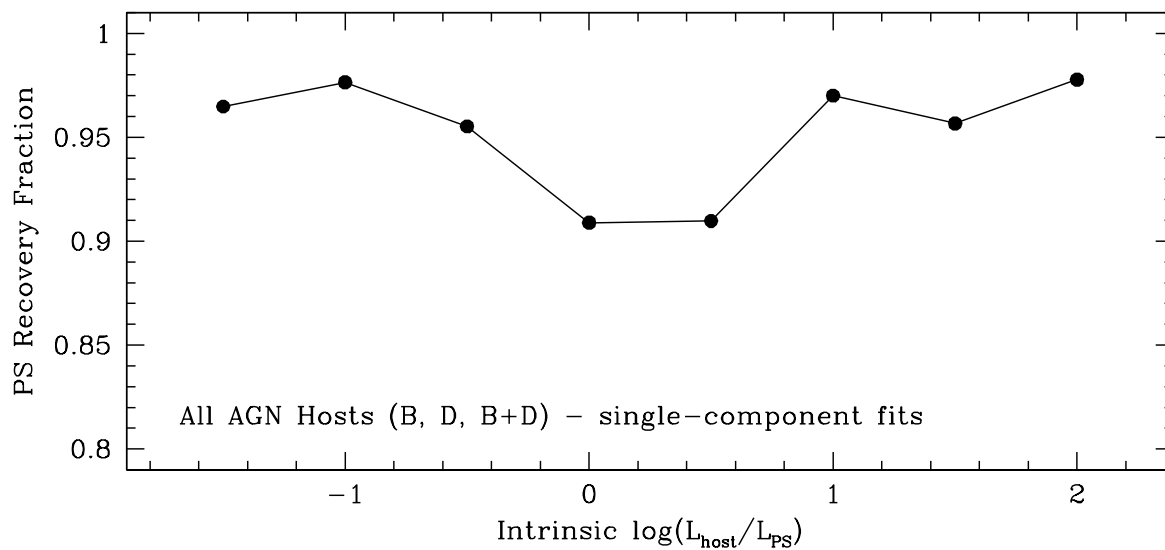


Fig. 14.— Fraction of point sources recovered for single-component fits to all simulated AGN host galaxies. The fraction of recovered point sources is slightly lower when the with input $\log(L_{\text{host}}/L_{\text{PS}})$ is near zero ($L_{\text{PS}} \approx L_{\text{host}}$ or slightly fainter). However, even in these cases, the fits detect at least 90% of point sources.

find a point source nearly one-quarter of the time when the simulated galaxy is a pure bulge. Because our total sample is composed of equal numbers of pure bulge and pure disk galaxies, this gives an overall false detection of a central point source in 12% of inactive galaxies. However, this effect is strongly dependent on morphology: fits to elliptical galaxies are far more likely to detect a faint point source when none are present than fits to disk galaxies. Host galaxy studies estimating the uncertainty in the fraction of hosts with detected optical point sources should therefore consider the morphological composition of their data sample: if the sample contains mostly elliptical galaxies, the number of false detections could be as high as 25%.

4.2.3. Redshift Effects on AGN Host Galaxies

At higher redshifts, surface-brightness dimming causes loss of extended components, and an unresolved central AGN corresponds to a larger fraction of a galaxy’s central region at high redshift for fixed spatial resolution. Because our GOODS data sample (S08), as well as those of others (Sánchez et al. 2004; Grogin et al. 2005; Ballo et al. 2007; Alonso-Herrero et al. 2008), extends to $z \approx 1$, we consider the quantitative effects of redshift on morphological classification.

After applying data cuts requiring $\Delta r_e \leq 90$ pixels and $|\Delta m_{tot}| \leq 0.5$ to our results at all redshifts, we assess the reliability of using the Sérsic index to classify single-component galaxies at different redshifts in Figure 16. We have “classified” a galaxy as bulge-dominated if it has $n > 2.0$ and disk-dominated if it has $n < 2.0$. Figure 16 then shows the fraction of correctly classified B- and D-type galaxies at each redshift. In general, the classification of pure bulges and pure disks is highly reliable for AGN host galaxies and point sources. At all redshifts, disks and bulges are correctly classified at least 90% of the time using these data cuts. Without these cuts, the misidentification rate increases to as much as 15%.

The average recovery of input half-light radius for all our simulated galaxies (pure bulges and disks as well as B+D bulges and disks) is shown in Figure 17. Each point represents the peak of the distribution of Δr_e values for a single galaxy type/component in each redshift bin. The error bars give the limits of the central 68% of data points; the peak of each distribution is generally not coincident with the numerical “center” of each bin. Single-component Sérsic fits to pure bulges and disks recover the radius reliably at all redshifts. Fitted radii to bulge and disk components in B+D hosts recover the intrinsic radius of the component to within 1 kpc on average; however, the errors are larger and these fits are more uncertain. For example, the width (containing 68% of sources) of the Δr_e distribution of $z \approx 1$ pure disks is less than 1 kpc, whereas the width of the $z \approx 1$ distribution of Δr_e for disk components in B+D hosts

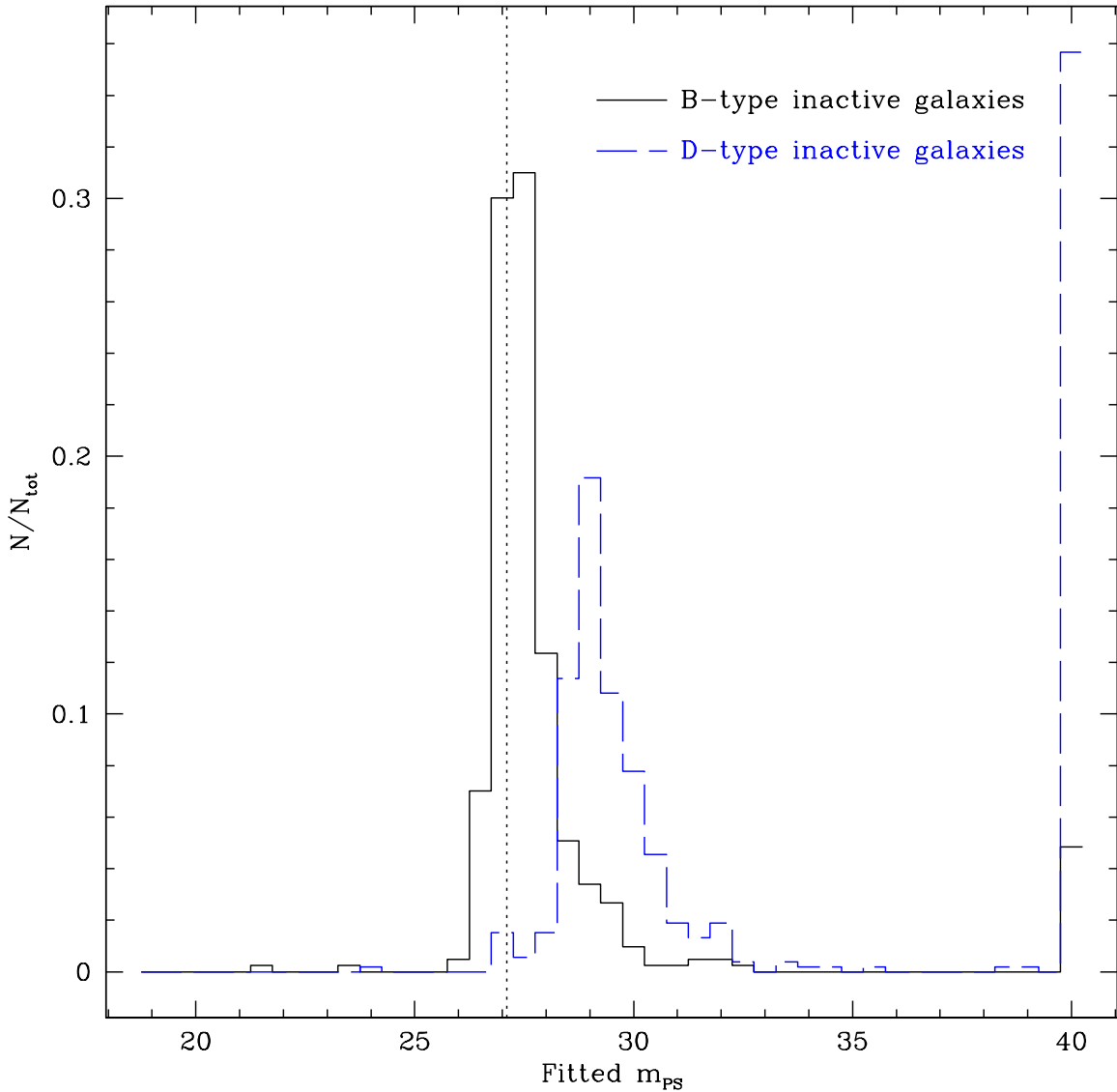


Fig. 15.— Distribution of fitted point-source magnitude for simulated *inactive* galaxies. Only 1% of pure disk inactive galaxies (blue dashed histogram) recovers point-source magnitudes brighter than the 10σ detection limit (dotted line) for the GOODS survey (from which our noise properties are taken). When the galaxy is a pure bulge (black histogram), however, a point source is found above the 10σ threshold in approximately 25% of fits. The overall percentage of fits where a point-source is found when none exists is 12% (for both pure bulges and pure disks combined), but this number is strongly dependent on intrinsic morphology.

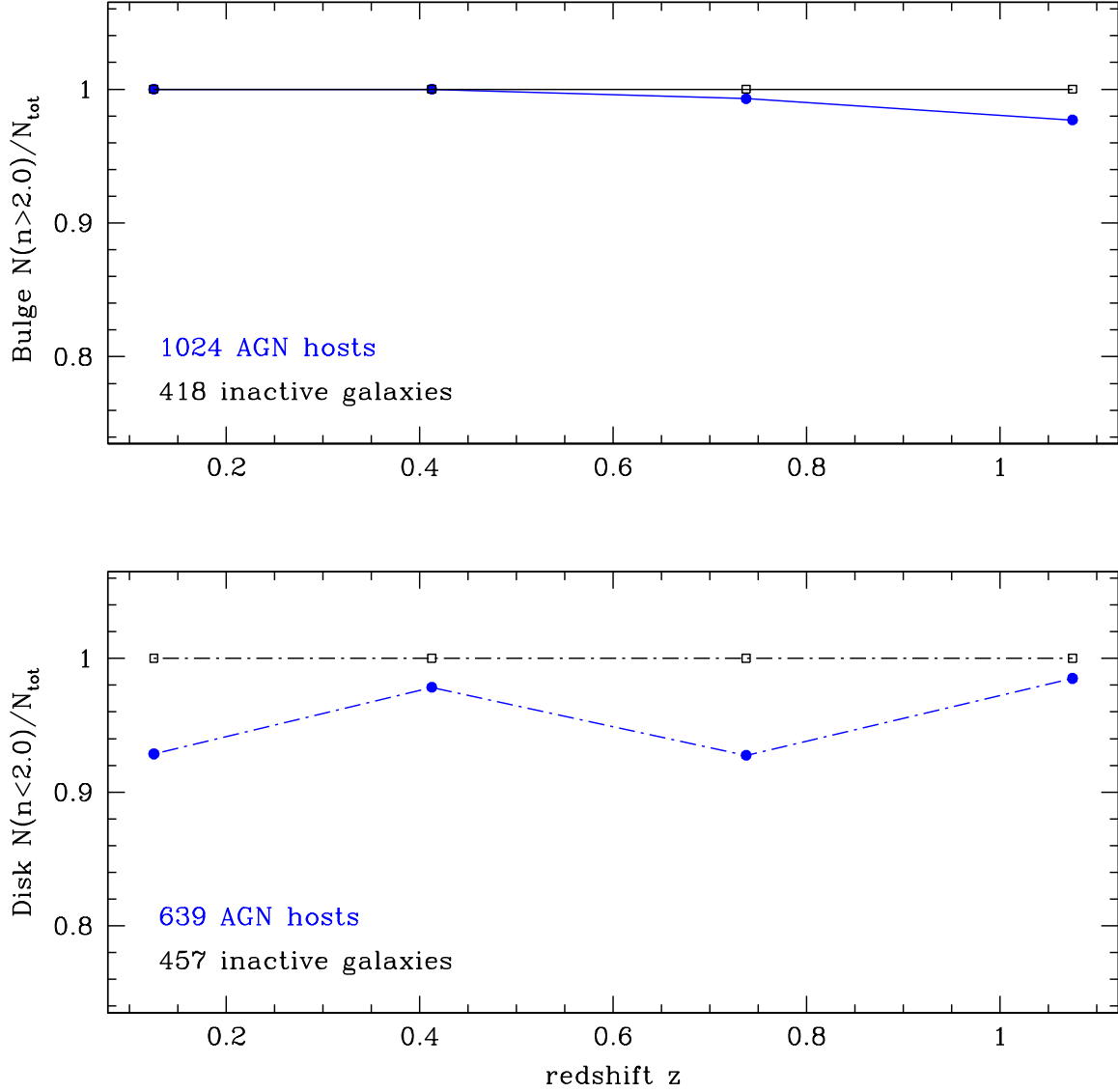


Fig. 16.— Dependence of galaxy classification on redshift for simulated bulge galaxies ($n_{\text{in}} = 4$; top, solid lines) and disk galaxies ($n_{\text{in}} = 1$; bottom, dot-dashed lines) with (blue) and without (black) central point sources. The y-axis is the fraction of galaxies correctly identified as bulges or disks given a threshold of $n > 2.0$ for bulge-dominated classification and $n < 2.0$ for a galaxy with a significant disk. Although we have here adopted a cutoff of $n = 2.0$, the results change by less than 5% when we change the cutoff to values between $1.5 < n < 3$.

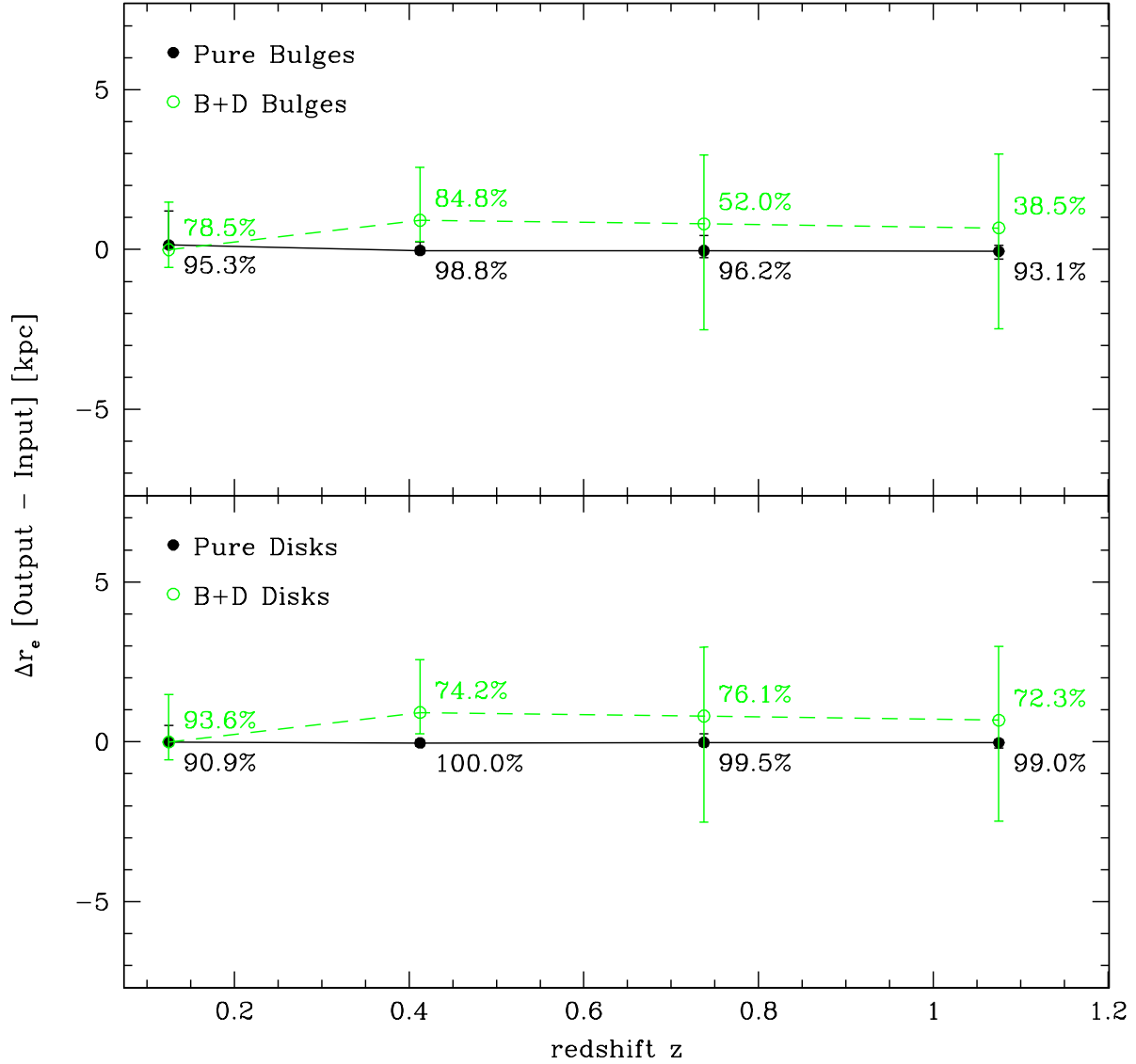


Fig. 17.— Recovery of input radii for pure and B+D bulges (top panel) and disks (bottom panel). Each point represents the peak of the distribution of single-component (black, solid lines) and two-component (green, dashed lines) Δr_e at each redshift. The numbers next to each point indicate the percentage of completed fits with $r_e > 5$ and $\Delta r_e \leq 90$ pixels, so that the fit converged to a physical value and would not be rejected by eye based on the fit residuals. While median fitted bulge and disk sizes are generally accurate to within 1 kpc at all redshifts, the presence of a central point source increases the spread in the distribution by up to a factor of 3. In addition, the majority of bulge fits within B+D galaxies at $z \approx 1$ are not able to converge to a sensible value for the bulge radius.

is approximately 3 kpc. Although the average recovery of bulge and disk component radii in B+D galaxies is accurate to within 1 kpc, individual radii are highly uncertain.

The percentage of sources remaining after removing fits with incorrect total magnitudes and unphysically low or high values of r_e , as previously discussed, is also shown for each bin in Figure 17. The number of fits for which the fitted $r_e < 5$ pixels remains relatively constant with redshift, but the number of fits for which the fitted r_e value diverges increases with redshift, more dramatically so for bulges than for disks. In the $z \approx 1$ sample, fewer than 40% of bulges within two-component fits have fitted radii within a reasonable physical range. This is likely due not just to the presence of the additional disk component, but also to the fact that the bulge is much smaller at higher redshift compared to the size of the central point source. In these cases, the bulge and the point source can be confused, often resulting in a divergent bulge fit. This happens less frequently for disks for two reasons: first, disks are generally more extended than bulges, and second, the radial profile of the ACS PSF more closely resembles that of a de Vaucouleurs bulge than an exponential disk.

Because different fractions of galaxies are removed from the sample at different redshifts (and for different bulge sizes), the morphological composition of a galaxy sample may be altered from its intrinsic composition simply by applying a reasonable cut on the morphological fit parameters, even if this cut is applied evenly (as it is in Figure 17).

Figure 18 thus shows the fitted morphological fraction of bulges with redshift of our simulated sample of pure bulges and disks for both AGN hosts and inactive galaxies. After applying the radius and magnitude cuts above (i.e., removing only unphysical fit results from the sample), we calculate the fraction of galaxies in each redshift bin that would be classified as bulge-dominated according to an $n > 2$ cut. For a perfectly-recovered sample, this fraction would be $N(n > 2.0)/N_{tot} = 0.5$ at all redshifts because we simulated equal numbers of bulges and disks. However, the convergence rate for pure bulge and disk fits is slightly different at each redshift, and even our set of reasonable and conservative error cuts removes different fractions of bulge and disk galaxies at each redshift. While this does affect the morphological composition of the sample at each redshift, its effect is small: the morphological fraction of $n > 2$ galaxies for AGN hosts is typically within 2% of the intrinsic fraction at all redshifts. The inactive galaxy morphological fraction is within 5% of the intrinsic fraction at all redshifts; both samples are consistent within their uncertainties with the intrinsic fraction.

For the two-component B+D galaxies, the dependence of fitted Sérsic index on input bulge-to-total ratio is shown in Figure 19. We see a general dependence of fitted n on the intrinsic bulge-to-total ratio. The relation changes somewhat as the sample is redshifted, but at all redshifts the Sérsic index indicates that galaxies may be fitted with a Sérsic index

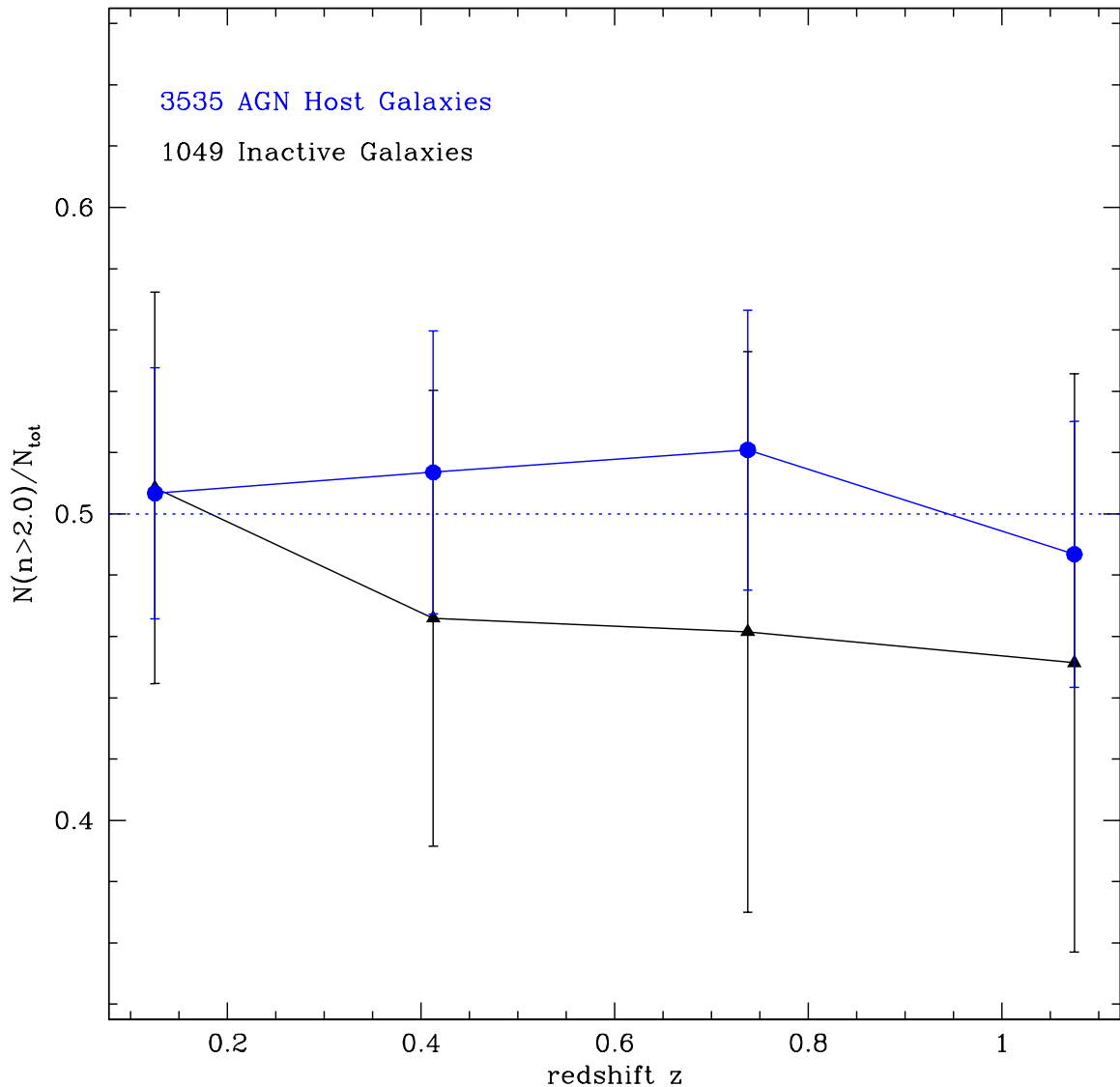


Fig. 18.— Fraction of galaxies classified as bulges with redshift. Blue circles represent simulated AGN hosts, and black triangles represent simulated inactive galaxies (error bars determined using Poisson statistics). Because the initial simulation contains equal numbers of pure bulges and disks, the actual bulge fraction is 0.5 for both samples. At the lowest redshift bin, these fractions are recovered to within 1% for both samples. The sample of simulated AGN host galaxies is mis-classified by up to 2% (0.02), and the inactive sample is mis-classified by up to 5%. Uncertainties are higher for inactive galaxies due to lower numbers of galaxies in the inactive sample, but in both cases the recovered fractions are consistent with the correct fraction within the uncertainties.

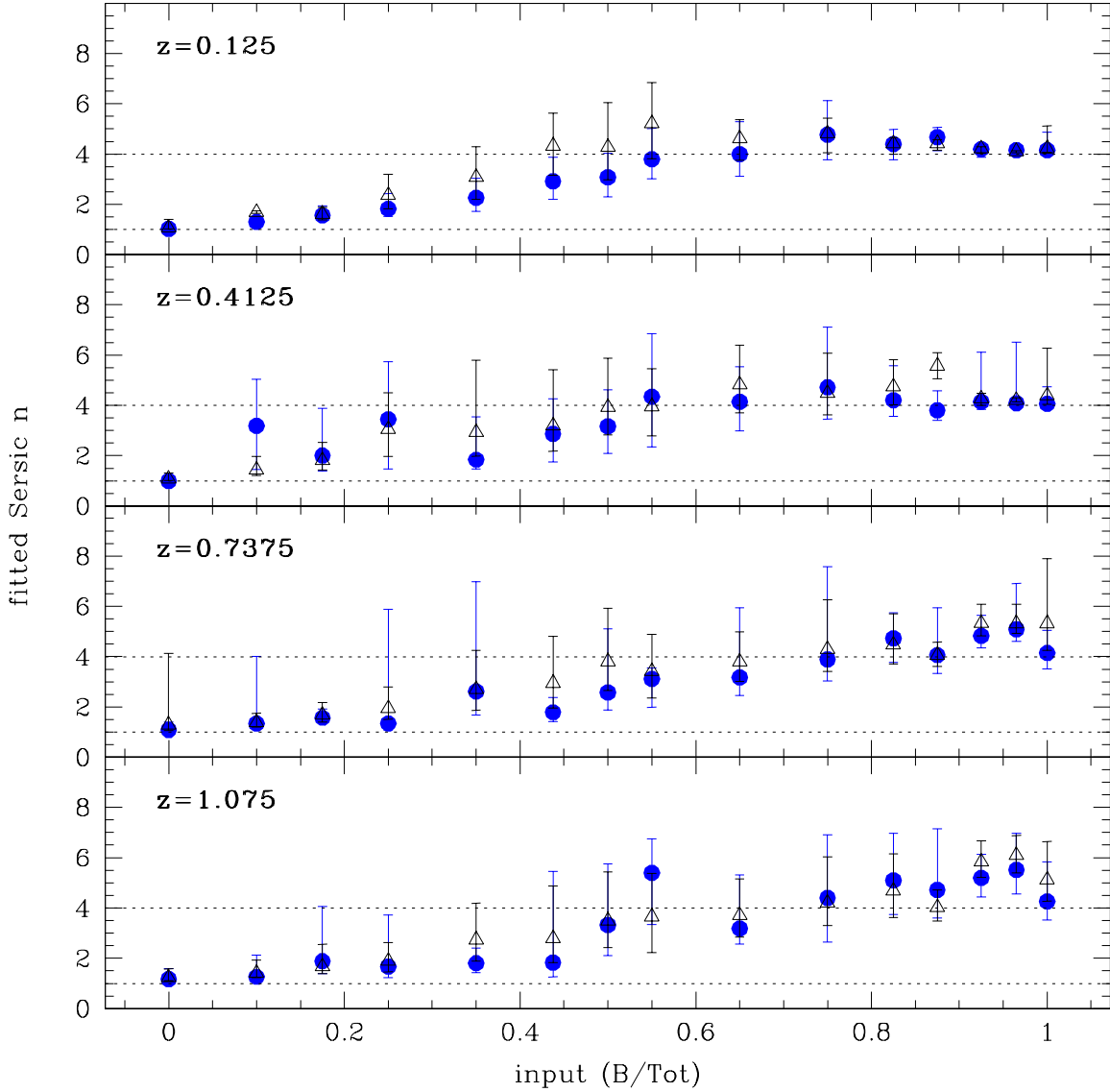


Fig. 19.— Fitted Sérsic index vs. input bulge-to-total ratio, for simulated normal galaxies (black triangles) and galaxies with added point sources (blue circles). At all redshifts (low to high, top to bottom) the fit correctly finds disks ($n = 1$) at $(L_B/L_{tot}) = 0$ and bulges ($n = 4$) at $(L_B/L_{tot}) = 1$. However, some galaxies fit to Sérsic values of $n \geq 4$ despite having up to 30% of their intrinsic light from a disk. Galaxies with intermediate values of n ($2 < n < 4$) likely have bulges that contribute between 20% and 70% of the total galaxy light. Points plotted are the median of each bin’s distribution; error bars mark the widths of each distribution enclosing the central 68% of sources in the bin.

indicative of a pure bulge ($n = 4$) even in cases where a disk is present and contributing up to 45% of the total galaxy light. However, a fitted Sérsic index consistent with an exponential disk ($n = 1$) typically indicates very little bulge contribution ($< 10\%$); galaxies fitted with $n < 1.5$ have $(L_B/L_{tot}) < 0.2$. Intermediate values of the Sérsic parameter, $1.5 < n < 3$, generally indicate a galaxy with both bulge and disk, but the bulge-to-total ratio may vary between $0.2 \leq (L_B/L_{tot}) \leq 0.65$, indicating that it is impossible to determine with a single-component fit whether a host galaxy with an intermediate Sérsic index is intrinsically bulge- or disk-dominated. Given that two-component B+D fits are also uncertain in the presence of a central point source, we conclude that determination of the bulge-to-total ratio is uncertain by at least 20% in AGN host galaxies, with a higher uncertainty for hosts with intermediate Sérsic indices and/or fitted (L_B/L_{tot}) .

Figure 20 shows the recovery of detected input point sources, hosts, and host-to-PS contrast ratios for our simulated galaxies (B, D, and B+D) at all redshifts. Again we see that for the local sample, the recovery is excellent: not only are point sources detected at least 95% of the time, but the recovered magnitude is typically within at least 0.1 ± 0.12 dex of the intrinsic magnitude. In fact, point-source recovery is very good at all redshifts: the recovered magnitude is within 0.5 dex of the input magnitude for all redshifts and input point-source magnitudes.

The dispersion in recovered values for the host galaxy magnitude is higher than that of point-source magnitude values for all redshifts. While in the local redshift bin the median recovered host magnitude is within 0.1 dex of the input magnitude, the central 68% of values has a larger spread. At higher redshifts, the host galaxy is more likely to converge to magnitudes that are too bright compared to the input magnitude. This effect is more pronounced for sources with a brighter input point source, as expected. For sources with a bright point source compared to the host, the difference is $\Delta m_{host} = 0.6$ for $z > 0.7$. For $z \approx 1$, the distribution of Δm_{host} has an extended tail to negative (too-bright) values: a significant fraction of high-redshift sources overestimates the host brightness by up to 1.8 dex regardless of the host-to-PS contrast ratio. For $z < 1$, this tail also exists for all host-to-PS values. However, when the input point source is faint compared to the host, the host magnitude is fitted to within $-0.8 < \Delta m_{host} < 0.3$ (1σ) for these redshifts.

5. Summary and Conclusions

We simulated 54,418 GOODS ACS galaxy images of inactive and AGN host galaxies at redshifts $0.125 < z < 1.25$, the largest sample of simulated two-dimensional galaxy morphologies to date.

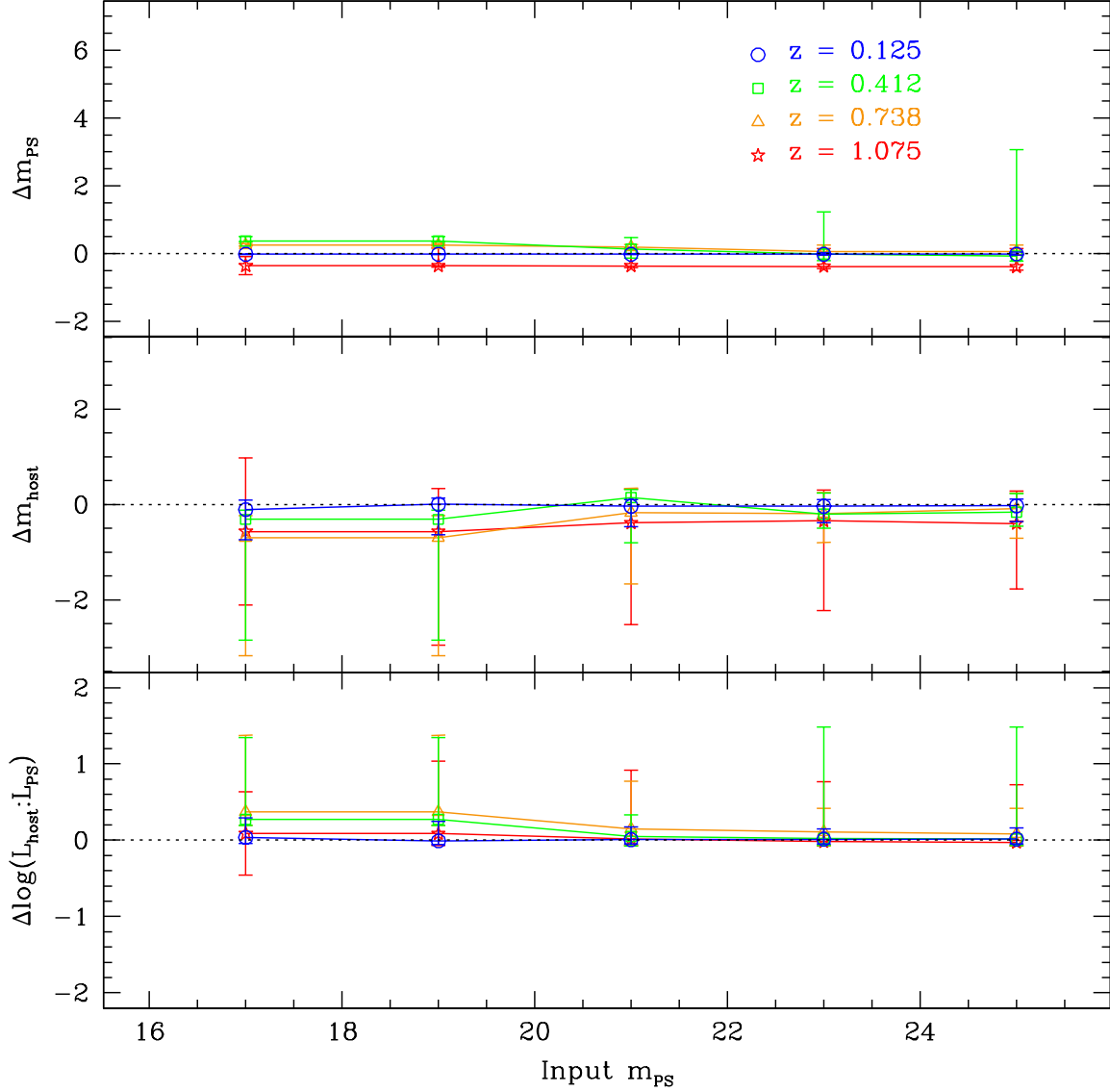


Fig. 20.— Effects of redshift on recovery of input point sources (top), input host magnitudes (middle), and host-to-PS contrast ratio, shown for all our simulated host galaxies. Each panel shows the fitted quantity versus the input point-source magnitude. Each line in a panel represents a different redshift bin: $z = 0.125$ (blue, circles), $z = 0.4125$ (green, squares), $z = 0.7375$ (orange, triangles), and $z = 1.075$ (red, stars).

Using a robust initial guess routine followed by batch-fitting, we performed single-component and bulge-disk host galaxy fits on these simulated galaxies, while also extracting the central point-source components of the AGN.

For batch-fit galaxies with central point-source components, typically 60%-70% of the fits converge successfully and pass our error cuts. This percentage can be significantly increased by follow-up case-by-case fitting, starting from the results of the batch fitting routines.

We reliably extract central point-source magnitudes for the simulated AGNs using a simple χ_ν^2 cut on the recovered fits. Using a combination $\chi_\nu^2 < 2$ and relative effective radius error cut of $(\sigma_{r_e}/r_e) = 0.8$ removes 88% of the poor host galaxy fits while excluding 12% of good host galaxy fits. The accurate extraction of AGN and host galaxy parameters does not depend on the host:AGN contrast ratio ($L_{\text{host}}/L_{\text{PS}}$), as long as it is greater than 1:4.

Galaxy size is recovered to within $\Delta r_e < 1$ kpc for single-component galaxies. For individual bulges and disks within two-component bulge + disk host galaxy fits, the distribution of recovered radii peaks within $\Delta r_e < 1$ kpc at all redshifts, but the large width of the distributions indicates that individual fits to bulges and disks within two-component galaxies are highly uncertain.

The average recovered morphological fraction of our sample is within 5% of the true fraction, even at $z \approx 1$. Of course, this number should be regarded as a lower limit since actual data samples of two-dimensional AGN host galaxy morphologies are likely to be significantly smaller than our simulations, and thus suffer from more uncertain statistics. We recover the correct morphology 99% of the time for inactive galaxies out to $z = 1.25$.

The average bulge-to-total ratios are within 10% of the true ratio at all redshifts, but with large scatter ($\sim 50\%$). This means that values for individual hosts are unreliable at the 50% level, but statistical population averages are more accurate. Thus, uncertainties in individual black hole masses determined using $L_{\text{bulge}} - M_{\text{BH}}$ relations (McLure & Dunlop 2002; Marconi & Hunt 2003; Ferrarese & Ford 2005) are higher when using fitted bulge luminosities of AGN host galaxies than those of inactive galaxies, and may be systematically overestimated due to the presence of central point sources.

Galaxies with Sérsic $n < 1.5$ are generally disk-dominated, with at least 80% of their total light coming from a disky component. Galaxies with intermediate $1.5 < n < 3$ have larger bulge components (occupying from 20% to 65% of the total galaxy light). Galaxies that appear to be bulge-dominated, i.e., with $n \geq 3$, may derive as little as 45% (depending on redshift) of their total light from a bulge component; for $n = 4$, typically $\sim 70\%$ of the galaxy light comes from the bulge.

In fully simulated AGN host galaxies, the central point source is correctly detected over 90% of the time, with only weak dependence on the intrinsic contrast ratio between the host galaxy and point source or the host morphology. This indicates that a sample of AGN host galaxy fits to ACS data with $z < 1.25$ is at least 90% complete in its detection of central point sources.

However, we also detect spurious point sources in simulated galaxies where no central point source is present, for as little as 1% or as high as 25% of the galaxies, depending on the morphological composition of the sample. Fits to bulge-dominated galaxies are far more likely to detect a point source when none are present than fits to disk-dominated galaxies.

We have used these simulations to evaluate the robustness of our results for AGN host galaxies observed with ACS. This is important for assessing the accuracy of recovered host morphologies, as well as the evolution of AGN host morphology with redshift. All of our results that can be quantitatively applied to a sample of real AGN host galaxies are also presented in tabular format (Tables 2, 3, and 4).

We have performed these simulations using the image depths and noise properties of GOODS, but they may also be used for other ACS surveys such as GEMS (Rix et al. 2004), COSMOS (Scoville et al. 2007), and AEGIS (Davis et al. 2007). The extent to which these simulations are directly applicable or provide limits on the accuracy of AGN host galaxy morphological fits for other ACS data depends on the relative depth of observations in each survey.

It is important to note that these results apply to redshifts where the ACS bands are observing rest-frame optical data, e.g. $z < 1.25$. As we move into the era of newer telescopes such as the *James Webb Space Telescope* and observing rest-frame optical wavelengths at very high resolution becomes possible for higher redshifts, an understanding of the effects of a central point source on high-redshift morphologies will become crucial. Simulations to probe these effects have begun on small scales (Dasyra et al. 2008), but more such work is needed.

The authors wish to thank C. Conselice, L. Moustakas, P. Natarajan, S. Ravindranath, and the entire GOODS team for helpful discussions that improved this work. Thanks especially to C. Peng for making GALFIT publicly available and for many enlightening discussions. We acknowledge support from NASA through grants HST-AR-10689.01-A, HST-GO-09425.13-A and HST-GO-09822.09-A from the Space Telescope Science Institute, which is operated by the Association of Universities for Research in Astronomy under NASA contract NAS 5-26555.

REFERENCES

- Alonso-Herrero, A., Pérez-González, P. G., Rieke, G. H., Alexander, D. M., Rigby, J. R., Papovich, C., Donley, J. L., & Rigopoulou, D. 2008, *ApJ*, 677, 127
- Ballo, L., Cristiani, S., Fasano, G., Fontanot, F., Monaco, P., Nonino, M., Pignatelli, E., Tozzi, P., Vanzella, E., Fontana, A., Giallongo, E., Grazian, A., & Danese, L. 2007, *ApJ*, 667, 97
- Bertin, E., & Arnouts, S. 1996, *A&AS*, 117, 393
- Binney, J., & Merrifield, M. 1998, *Galactic astronomy* (Galactic astronomy / James Binney and Michael Merrifield. Princeton, NJ : Princeton University Press, 1998. (Princeton series in astrophysics) QB857 .B522 1998 (\$35.00))
- Conselice, C. J. 2003, *ApJS*, 147, 1
- Dasyra, K. M., Yan, L., Helou, G., Surace, J., Sajina, A., & Colbert, J. 2008, *ArXiv e-prints*, 802
- Davis, M., Guhathakurta, P., Konidakis, N. P., Newman, J. A., Ashby, M. L. N., Biggs, A. D., Barmby, P., Bundy, K., Chapman, S. C., Coil, A. L., Conselice, C. J., Cooper, M. C., Croton, D. J., Eisenhardt, P. R. M., Ellis, R. S., Faber, S. M., Fang, T., Fazio, G. G., Georgakakis, A., Gerke, B. F., Goss, W. M., Gwyn, S., Harker, J., Hopkins, A. M., Huang, J.-S., Ivison, R. J., Kassin, S. A., Kirby, E. N., Koekemoer, A. M., Koo, D. C., Laird, E. S., Le Floc’h, E., Lin, L., Lotz, J. M., Marshall, P. J., Martin, D. C., Metevier, A. J., Moustakas, L. A., Nandra, K., Noeske, K. G., Papovich, C., Phillips, A. C., Rich, R. M., Rieke, G. H., Rigopoulou, D., Salim, S., Schiminovich, D., Simard, L., Smail, I., Small, T. A., Weiner, B. J., Willmer, C. N. A., Willner, S. P., Wilson, G., Wright, E. L., & Yan, R. 2007, *ApJ*, 660, L1
- Ferrarese, L., & Ford, H. 2005, *Space Science Reviews*, 116, 523
- Ferrarese, L., & Merritt, D. 2000, *ApJ*, 539, L9
- Gebhardt, K., Bender, R., Bower, G., Dressler, A., Faber, S. M., Filippenko, A. V., Green, R., Grillmair, C., Ho, L. C., Kormendy, J., Lauer, T. R., Magorrian, J., Pinkney, J., Richstone, D., & Tremaine, S. 2000, *ApJ*, 539, L13
- Giavalisco, M., Ferguson, H. C., Koekemoer, A. M., Dickinson, M., Alexander, D. M., Bauer, F. E., Bergeron, J., Biagetti, C., Brandt, W. N., Casertano, S., Cesarsky, C., Chatzichristou, E., Conselice, C., Cristiani, S., Da Costa, L., Dahlen, T., de Mello,

- D., Eisenhardt, P., Erben, T., Fall, S. M., Fassnacht, C., Fosbury, R., Fruchter, A., Gardner, J. P., Grogin, N., Hook, R. N., Hornschemeier, A. E., Idzi, R., Joglee, S., Kretchmer, C., Laidler, V., Lee, K. S., Livio, M., Lucas, R., Madau, P., Mobasher, B., Moustakas, L. A., Nonino, M., Padovani, P., Papovich, C., Park, Y., Ravindranath, S., Renzini, A., Richardson, M., Riess, A., Rosati, P., Schirmer, M., Schreier, E., Somerville, R. S., Spinrad, H., Stern, D., Stiavelli, M., Strolger, L., Urry, C. M., Vandame, B., Williams, R., & Wolf, C. 2004, *ApJ*, 600, L93
- Graham, A. W. 2001, *AJ*, 121, 820
- Grogin, N. A., Conselice, C. J., Chatzichristou, E., Alexander, D. M., Bauer, F. E., Hornschemeier, A. E., Joglee, S., Koekemoer, A. M., Laidler, V. G., Livio, M., Lucas, R. A., Paolillo, M., Ravindranath, S., Schreier, E. J., Simmons, B. D., & Urry, C. M. 2005, *ApJ*, 627, L97
- Häussler, B., McIntosh, D. H., Barden, M., Bell, E. F., Rix, H.-W., Borch, A., Beckwith, S. V. W., Caldwell, J. A. R., Heymans, C., Jahnke, K., Joglee, S., Kopesov, S. E., Meisenheimer, K., Sánchez, S. F., Somerville, R. S., Wisotzki, L., & Wolf, C. 2007, *ApJS*, 172, 615
- Joglee, S., Barazza, F. D., Rix, H.-W., Shlosman, I., Barden, M., Wolf, C., Davies, J., Heyer, I., Beckwith, S. V. W., Bell, E. F., Borch, A., Caldwell, J. A. R., Conselice, C. J., Dahlen, T., Häussler, B., Heymans, C., Jahnke, K., Knapen, J. H., Laine, S., Lubell, G. M., Mobasher, B., McIntosh, D. H., Meisenheimer, K., Peng, C. Y., Ravindranath, S., Sanchez, S. F., Somerville, R. S., & Wisotzki, L. 2004, *ApJ*, 615, L105
- Koekemoer, A. M., Fruchter, A. S., Hook, R. N., & Hack, W. 2002, in *The 2002 HST Calibration Workshop : Hubble after the Installation of the ACS and the NICMOS Cooling System*, Proceedings of a Workshop held at the Space Telescope Science Institute, Baltimore, Maryland, October 17 and 18, 2002. Edited by Santiago Arribas, Anton Koekemoer, and Brad Whitmore. Baltimore, MD: Space Telescope Science Institute, 2002., p.339, 339–+
- Kormendy, J., & Richstone, D. 1995, *ARA&A*, 33, 581
- Magorrian, J., Tremaine, S., Richstone, D., Bender, R., Bower, G., Dressler, A., Faber, S. M., Gebhardt, K., Green, R., Grillmair, C., Kormendy, J., & Lauer, T. 1998, *AJ*, 115, 2285
- Marconi, A., & Hunt, L. K. 2003, *ApJ*, 589, L21
- Marleau, F. R., & Simard, L. 1998, *ApJ*, 507, 585

- McLure, R. J., & Dunlop, J. S. 2002, MNRAS, 331, 795
- Peng, C. Y., Ho, L. C., Impey, C. D., & Rix, H.-W. 2002, AJ, 124, 266
- Ravindranath, S., Ferguson, H. C., Conselice, C., Giavalisco, M., Dickinson, M., Chatzichristou, E., de Mello, D., Fall, S. M., Gardner, J. P., Grogin, N. A., Hornschemeier, A., Joglee, S., Koekemoer, A., Kretchmer, C., Livio, M., Mobasher, B., & Somerville, R. 2004, ApJ, 604, L9
- Rix, H.-W., Barden, M., Beckwith, S. V. W., Bell, E. F., Borch, A., Caldwell, J. A. R., Häussler, B., Jahnke, K., Joglee, S., McIntosh, D. H., Meisenheimer, K., Peng, C. Y., Sanchez, S. F., Somerville, R. S., Wisotzki, L., & Wolf, C. 2004, ApJS, 152, 163
- Sánchez, S. F., Jahnke, K., Wisotzki, L., McIntosh, D. H., Bell, E. F., Barden, M., Beckwith, S. V. W., Borch, A., Caldwell, J. A. R., Häussler, B., Joglee, S., Meisenheimer, K., Peng, C. Y., Rix, H.-W., Somerville, R. S., & Wolf, C. 2004, ApJ, 614, 586
- Scoville, N., Aussel, H., Brusa, M., Capak, P., Carollo, C. M., Elvis, M., Giavalisco, M., Guzzo, L., Hasinger, G., Impey, C., Kneib, J.-P., LeFevre, O., Lilly, S. J., Mobasher, B., Renzini, A., Rich, R. M., Sanders, D. B., Schinnerer, E., Schminovich, D., Shopbell, P., Taniguchi, Y., & Tyson, N. D. 2007, ApJS, 172, 1
- Sérsic, J. L. 1968, Atlas de galaxias australes (Cordoba, Argentina: Observatorio Astronomico, 1968)
- Sheth, K., Elmegreen, D. M., Elmegreen, B. G., Capak, P., Abraham, R. G., Athanassoula, E., Ellis, R. S., Mobasher, B., Salvato, M., Schinnerer, E., Scoville, N. Z., Spalsbury, L., Strubbe, L., Carollo, M., Rich, M., & West, A. A. 2008, ApJ, 675, 1141
- Simard, L., Koo, D. C., Faber, S. M., Sarajedini, V. L., Vogt, N. P., Phillips, A. C., Gebhardt, K., Illingworth, G. D., & Wu, K. L. 1999, ApJ, 519, 563
- Spergel, D. N., Verde, L., Peiris, H. V., Komatsu, E., Nolta, M. R., Bennett, C. L., Halpern, M., Hinshaw, G., Jarosik, N., Kogut, A., Limon, M., Meyer, S. S., Page, L., Tucker, G. S., Weiland, J. L., Wollack, E., & Wright, E. L. 2003, ApJS, 148, 175
- Trujillo, I., & Aguerri, J. A. L. 2004, MNRAS, 355, 82

	Pure Bulges	Pure Disks	Bulge + Disk	
			<i>Bulge</i>	<i>Disk</i>
m_{gal} (I_{AB}, L_*)	16.898, 5.0	16.898, 5.0	16.898, 5.0	16.898, 5.0
	18.645, 1.0	18.645, 1.0	18.645, 1.0	18.645, 1.0
	19.398, 0.5	19.398, 0.5	19.398, 0.5	19.398, 0.5
	20.393, 0.2	20.393, 0.2	20.393, 0.2	20.393, 0.2
			20.750, 0.14	20.750, 0.14
r_e (pixels, kpc)	13.54, 1.5	36.12, 4.0	27.09, 3.0	54.18, 6.0
	27.09, 3.0	54.18, 6.0	40.63, 4.5	72.23, 8.0
	40.63, 4.5	72.23, 8.0	54.18, 6.0	90.29, 10.0
	54.18, 6.0	90.09, 10.0		
b/a	0.25	0.25	0.65	0.30
	0.50	0.50	1.0	0.65
	0.75	0.75		1.0
	1.0	1.0		
PA (degrees)	45.0	45.0	45.0	45.0
			60.0	
m_{PS} (I_{AB})	none	none	none	
	16.500	16.500	16.500	
	18.375	18.375	20.250	
	20.250	20.250	22.125	
	22.125	22.125		
	24.000	24.000		

Table 1: Grid values for simulated galaxies at $z = 0.125$. The effective radius r_e values differ between the bulge and disk galaxies due to the different physical sizes of these two classes of galaxies. The parameter space varies slightly between single-component galaxies and double-component galaxies in order to increase the number of mesh points in the bulge-to-total ratio without increasing the simulated double-component galaxies to a computationally prohibitive number. Conversion from magnitude to luminosity and between pixels and physical size uses a concordance cosmology ($\Omega_{tot} = 1$, $\Omega_\Lambda = 0.73$, and $H_0 = 71$ km/s/Mpc) and a redshift $z = 0.125$.

Source	m_{PS}	N_{conv}	$\sigma_{m_{PS}}$	N_1	$\sigma_{m_{host}}$	σ_n	σ_{r_e}	N_2
(AB)							(pixels)	
21		374	0.33	210	1.09	2.10	15.6	45
22		389	0.48	273	0.12	0.97	21.8	85
23		397	0.27	359	0.15	0.67	11.0	138
24		394	0.15	328	0.20	0.54	26.7	184
25		382	0.17	328	0.14	0.40	15.9	223
26		372	0.27	295	0.17	0.44	8.2	215
27		355	0.47	271	0.12	0.27	7.9	215
28		315	0.87	228	0.10	0.22	6.3	192
29		286	1.20	193	0.09	0.27	1.6	161

Table 2: RMS values for fit parameters vary with central point-source magnitude. N_{conv} is the number of fits which converged (out of 450) for each input point-source magnitude value. N_1 is the number remaining after applying a $\chi^2_\nu < 2.0$ cut; N_2 is the number remaining after further requiring $\sigma_{r_e}/r_e < 0.8$. The RMS value for the point-source magnitude is calculated from N_1 galaxies, and the values for $\sigma_{m_{host}}$, σ_n , and σ_r are calculated from N_2 objects. *Note:* Results for these magnitudes are based on a survey with the GOODS depths (Giavalisco et al. 2004).

Source	$\log(L_{host}/L_{PS})$	$\sigma_{m_{PS}}$	$\sigma_{m_{host}}$	σ_n	σ_{r_e}
					(pixels)
	-1.5	0.26	0.78	0.70	7.2
	-1.0	0.31	0.29	0.38	6.2
	-0.5	0.31	0.31	0.31	7.1
	0.0	0.36	0.35	0.27	5.4
	0.5	1.69	0.32	0.24	4.4
	1.2	1.92	0.23	0.33	4.6
	1.9	0.69	0.07	0.20	3.4

Table 3: Determined RMS values for fit parameters to sources with different $\log(L_{host}/L_{PS})$.

Fitted Sérsic index	Intrinsic bulge-to-total ratio
$n \leq 1.5$	$(B/Tot) < 0.2$
$1.5 < n < 3$	$0.2 < (B/Tot) < 0.65$
$n \geq 3$	$(B/Tot) > 0.45$
$n \geq 4$	$(B/Tot) > 0.55$

Table 4: Relationship of a host galaxy’s fitted Sérsic index to its intrinsic bulge-to-total light ratio. Hosts with intermediate Sérsic index may have a wide range of bulge-to-total ratios; hosts with fitted $n = 4$, typically classified as pure deVaucouleur bulges, may in fact have bulge-to-total ratios as low as 55%.